The Astrophysical Journal, 902:47 (25pp), 2020 October 10 https://doi.org/10.3847/1538-4357/abb13b

ZTF Early Observations of Type Ia Supernovae. II. First Light, the Initial Rise, and Time to Reach Maximum Brightness

A. A. Miller[1,2], Y. Yao[3], M. Bulla[4], C. Pankow[1], E. C. Bellm[5], S. B. Cenko[6,7], R. Dekany[8], C. Fremling[3], M. J. Graham[9], T. Kupfer[10], R. R. Laher[11], A. A. Mahabal[9,12], F. J. Masci[11], P. E. Nugent[13,14], R. Riddle[8], B. Rusholme[11], R. M. Smith[8], D. L. Shupe[11], J. van Roestel[9], and S. R. Kulkarni[3]

[1] Center for Interdisciplinary Exploration and Research in Astrophysics and Department of Physics and Astronomy, Northwestern University, 1800 Sherman Ave, Evanston, IL 60201, USA; amiller@northwestern.edu
[2] The Adler Planetarium, Chicago, IL 60605, USA
[3] Cahill Center for Astrophysics, California Institute of Technology, 1200 E. California Boulevard, Pasadena, CA 91125, USA
[4] Nordita, KTH Royal Institute of Technology and Stockholm University, Roslagstullsbacken 23, SE-106 91 Stockholm, Sweden
[5] DIRAC Institute, Department of Astronomy, University of Washington, 3910 15th Avenue NE, Seattle, WA 98195, USA
[6] Astrophysics Science Division, NASA Goddard Space Flight Center, 8800 Greenbelt Road, Greenbelt, MD 20771, USA
[7] Joint Space-Science Institute, University of Maryland, College Park, MD 20742, USA
[8] Caltech Optical Observatories, California Institute of Technology, Pasadena, CA 91125, USA
[9] Division of Physics, Mathematics, and Astronomy, California Institute of Technology, Pasadena, CA 91125, USA
[10] Kavli Institute for Theoretical Physics, University of California, Santa Barbara, CA 93106, USA
[11] IPAC, California Institute of Technology, 1200 E. California Blvd, Pasadena, CA 91125, USA
[12] Center for Data Driven Discovery, California Institute of Technology, Pasadena, CA 91125, USA
[13] Computational Cosmology Center, Lawrence Berkeley National Laboratory, 1 Cyclotron Road, Berkeley, CA 94720, USA
[14] Department of Astronomy, University of California, Berkeley, CA 94720-3411, USA
Received 2020 January 17; revised 2020 August 4; accepted 2020 August 6; published 2020 October 9

Abstract

While it is clear that Type Ia supernovae (SNe) are the result of thermonuclear explosions in C/O white dwarfs (WDs), a great deal remains uncertain about the binary companion that facilitates the explosive disruption of the WD. Here, we present a comprehensive analysis of a large, unique data set of 127 SNe Ia with exquisite coverage by the Zwicky Transient Facility (ZTF). High-cadence (six observations per night) ZTF observations allow us to measure the SN rise time and examine its initial evolution. We develop a Bayesian framework to model the early rise as a power law in time, which enables the inclusion of priors in our model. For a volume-limited subset of normal SNe Ia, we find that the mean power-law index is consistent with 2 in the $r_{\rm ZTF}$-band ($\alpha_r = 2.01 \pm 0.02$), as expected in the expanding fireball model. There are, however, individual SNe that are clearly inconsistent with $\alpha_r = 2$. We estimate a mean rise time of 18.9 days (with a range extending from ∼15 to 22 days), though this is subject to the adopted prior. We identify an important, previously unknown, bias whereby the rise times for higher-redshift SNe within a flux-limited survey are systematically underestimated. This effect can be partially alleviated if the power-law index is fixed to $\alpha = 2$, in which case we estimate a mean rise time of 21.7 days (with a range from ∼18 to 23 days). The sample includes a handful of rare and peculiar SNe Ia. Finally, we conclude with a discussion of lessons learned from the ZTF sample that can eventually be applied to observations from the Vera C. Rubin Observatory.

Unified Astronomy Thesaurus concepts: Type Ia supernovae (1728); Surveys (1671); Catalogs (205); Observational astronomy (1145); Supernovae (1668)

Supporting material: machine-readable tables

1. Introduction

The fact that supernovae (SNe) of Type Ia can be empirically calibrated as standardizable candles has made them arguably the most important tool in all of physics for the past ∼two decades. By unlocking our ability to accurately measure distances at high redshift, SNe Ia have revolutionized our understanding of the universe (Riess et al. 1998; Perlmutter et al. 1999).

While it is all but certain that SNe Ia are the result of thermonuclear explosions in carbon–oxygen (C/O) white dwarfs (WDs) in binary star systems (see Maoz et al. 2014; Livio & Mazzali 2018), there remains a great deal about SNe Ia progenitors and the precise explosion mechanism that we do not know. This leads to the tantalizing hope that an improved understanding of the binary companions or explosion may improve our ability to calibrate these standardizable candles.

Pinning down the binary companion to the exploding WD remains particularly difficult. There are likely two dominant pathways toward explosion. In the first, the WD accretes H or He from, or merges with the core of, a nondegenerate companion and eventually explodes as it approaches the Chandrasekhar mass ($M_{\rm Ch}$; known as the single degenerate, or SD, scenario (Whelan & Iben 1973)). In the second scenario, the explosion follows the interaction or merger of two WD stars (known as the double degenerate, or DD, scenario (Webbink 1984)). While the debate has long focused on which of these two scenarios is correct, empirical evidence supports both channels. PTF 11kx, an extreme example of a SN Ia, showed evidence of multiple shells of H-rich circumstellar material (Dilday et al. 2012), which is precisely what one would expect in a WD+red giant system that had undergone multiple novae prior to the final, fatal thermonuclear explosion (see Soker et al. (2013) for an alternative explanation for PTF 11kx). On the other hand, hypervelocity WDs discovered by Gaia are likely the surviving companions of DD explosions (Shen et al. 2018).

Recent observational evidence also challenges the canonical picture that WDs only explode near, or in excess of, $M_{\rm Ch}$. Detailed modeling of SNe Ia light curves (Scalzo et al. 2014) and a blue-to-red-to-blue color evolution observed in a few SNe (Jiang et al. 2017; De et al. 2019; Bulla et al. 2020), point to sub-$M_{\rm Ch}$ mass explosions. Such explosions are possible if a C/O WD accretes and retains a thick He shell. A detonation in this shell can trigger an explosion in the C/O core of the WD (e.g., Nomoto 1982a, 1982b).

Now the most pressing questions are the following: which binary companion WD (DD) or nondegenerate star (SD), and which mass explosion, $M_{\rm Ch}$ or sub-$M_{\rm Ch}$, is dominant in the production of normal SNe Ia?

Observing SNe Ia in the hours to days after explosion provides a clear avenue toward addressing these pressing questions (e.g., Maoz et al. 2014). Finding an SN during this early phase probes the progenitor environment and the binary companion, which is simply not possible once the SN evolves well into the expansion phase (they are standardizable precisely because they are all nearly identical at maximum light). Indeed, in the landmark discovery of SN 2011fe, Nugent et al. (2011) were able to constrain the time of explosion to ±20 minutes—though see Piro & Nakar (2013, 2014) for an explanation of a potential early "dark phase." Bloom et al. (2012) would later combine the observations in Nugent et al. (2011) with an early nondetection while comparing the limits to shock-breakout models to constrain the size of the progenitor to be $\lesssim 0.01\,R_\odot$, providing the most direct evidence to date that SNe Ia come from WDs.

Early observations also probe the nature of the binary system. In the SD scenario, the SN ejecta will collide with the nondegenerate companion, creating a shock that gives rise to a bright ultraviolet/optical flash in the days after explosion (Kasen 2010). To date, the search for such a signature in large samples has typically resulted in a nondetection (e.g., Hayden et al. 2010; Bianco et al. 2011; Ganeshalingam et al. 2011).[15] Separately, for the DD scenario, some sub-$M_{\rm Ch}$ DD explosions exhibit a highly unusual color evolution in the ∼2–4 days after explosion (Noebauer et al. 2017; Polin et al. 2019).

Furthermore, measurements of the SN rise time constrain the properties of the WD and the explosion. In combination with the peak bolometric luminosity, the rise time provides a direct estimate of the ejecta mass (e.g., Arnett 1982; Jeffery 1999). Regarding the explosions, initial work to estimate the rise times of SNe Ia clearly demonstrated that early models significantly underestimated the opacities in the SN ejecta (e.g., Riess et al. 1999). Finally, while the famous luminosity–decline relationship for SNe Ia makes them standardizable (Phillips 1993), recent evidence suggests that the rise, rather than the decline, of SNe Ia is a better indicator of their peak luminosity (Hayden et al. 2019).

To date, we have not reached a consensus on the typical rise time of SNe Ia. In their seminal study, Riess et al. (1999) found that the mean rise time of SNe Ia is 19.5 ± 0.2 days, after correcting the individual SNe for the luminosity–decline relation (we hereafter refer to these corrections as shape corrections). Follow-up studies estimated a similar mean rise time for high-redshift SNe Ia (Aldering et al. 2000; Conley et al. 2006).[16] In Hayden et al. (2010), Ganeshalingam et al. (2011), and González-Gaitán et al. (2012), similar approaches were applied to significantly larger samples of SNe, and shorter (by $\gtrsim$1 day) shape-corrected mean rise times were found.

As observational cadences have increased over the past decade, there has been a surge of SNe Ia discovered shortly after explosion. This has led more recent efforts to focus on measuring the rise times of populations of individual SNe (e.g., Firth et al. 2015; Zheng et al. 2017; Papadogiannakis et al. 2019), which is the approach adopted in this study. The utility of avoiding shape corrections is that it allows one to search for multiple populations in the distribution of rise times, which could point to a multitude of explosion scenarios. While Papadogiannakis et al. (2019) found no evidence for multiple populations, Ganeshalingam et al. (2011) found that high-velocity SNe Ia rise ∼1.5 days faster than their normal counterparts.

We are now in an era where hydrodynamic radiation transport models have become very sophisticated (e.g., Sim et al. 2013; Dessart et al. 2014; Kromer et al. 2016; Noebauer et al. 2017; Polin et al. 2019; Townsley et al. 2019; Gronow et al. 2020; Magee et al. 2020). Accurate measurements of the observed distribution of SN Ia rise times can be compared with models to rule out theoretical scenarios that evolve too quickly or too slowly (e.g., Magee et al. 2018). Similarly, if the early emission is modeled as a power law in time (i.e., $f \propto t^{\alpha}$), measures of the power-law index α can confirm or reject different explosion/ejecta-mixing scenarios (Magee et al. 2020).

In this paper, the second in a series of three examining the photometric evolution of 127 SNe Ia with early observations discovered by the Zwicky Transient Facility (ZTF; Bellm et al. 2019b; Graham et al. 2019; Dekany et al. 2020) in 2018, we examine the rise time of SNe Ia and whether or not their early emission can be characterized as a simple power law. Paper I (Yao et al. 2019) describes the sample, while Paper III (Bulla et al. 2020) discusses the color evolution of SNe Ia shortly after explosion. The sample, which is large, is equally impressive in its quality: ZTF observations are obtained in both the $g_{\rm ZTF}$ and $r_{\rm ZTF}$ filters every night. The nightly cadence and multiple filters are essential to constrain the distribution of ^{56}Ni in the SN ejecta (e.g., Magee et al. 2020). Conducting the search with the same telescope that provides follow-up observations enables subthreshold detections (Yao et al. 2019), separating the ZTF sample from other low-z data sets. We construct a Bayesian framework to estimate the rise time of individual SNe. This approach allows us to naturally incorporate priors into the model fitting. We uncover a systematic bias whereby the rise times of the higher-redshift SNe within a flux-limited survey are typically underestimated. We show that the adoption of strong priors can, at least partially, alleviate this bias. Finally, we conclude with a

[15] There are claims of companion interaction based on short-lived optical "bumps" in the early light curves of individual SNe (e.g., Cao et al. 2015; Marion et al. 2016; Hosseinzadeh et al. 2017; Dimitriadis et al. 2019). Alternative models (e.g., Dessart et al. 2014; Piro & Morozova 2016; Levanon & Soker 2017; Polin et al. 2019; Magee & Maguire 2020) utilizing different physical scenarios can produce similar bumps, leading many (e.g., Kromer et al. 2016; Noebauer et al. 2017; Miller et al. 2018, 2020; Shappee et al. 2018, 2019) to appeal to alternative explanations to ejecta–companion interaction.

[16] Aldering et al. (2000) importantly point out that rise time estimates can be significantly biased if uncertainties in the time of maximum light are ignored.

discussion of lessons from ZTF that can be applied to the Vera C. Rubin Observatory Legacy Survey of Space and Time (LSST).

Along with this paper, we have released our open-source analysis for this study. It is available online at https://github.com/adamamiller/ztf_early_Ia_2018.

2. ZTF Photometry

Yao et al. (2019) provide detailed selection criteria for the 127 SNe Ia utilized in Papers I, II, and III in this series on early observations of ZTF SNe Ia. In summary, these 127 SNe were observed as part of the high-cadence extragalactic experiment conducted by the ZTF partnership in 2018 (Bellm et al. 2019a). This experiment monitors $\sim$3000 deg^2 on a nightly basis (over the nine month period when the fields are visible), with the aim of obtaining three $g_{\rm ZTF}$ and three $r_{\rm ZTF}$ observations every night. In total, there were 247 spectroscopically confirmed SNe Ia discovered within these fields, as tabulated by the GROWTH Marshal (Kasliwal et al. 2019). Following cuts to limit the sample to SNe that were discovered "early" (defined as 10 days or more, in the SN rest frame, prior to the time of maximum light in the Bband, $T_{B,\rm max}$) and have high-quality light curves, the sample was reduced to 127 SNe; see Yao et al. (2019) for the full details.

In Yao et al. (2019), we produced "forced" point-spread function (PSF) photometry for each of the 127 SNe on every image covering the position of the SN. The PSF model was generated as part of the ZTF real-time image subtraction pipeline (Masci et al. 2019), which uses an image-differencing technique based on Zackay et al. (2016). The forced PSF photometry procedure fixes the position of each SN and measures the PSF flux in all images that contain the SN position, even in epochs where the signal-to-noise ratio (S/N) $\lesssim 1$ and the SN is not detected.

We normalize the SN flux relative to the observed peak flux in the $g_{\rm ZTF}$ and $r_{\rm ZTF}$ bands as measured by SALT2 (Guy et al. 2007); see Yao et al. (2019) for our SALT2 implementation details. The relative fluxes produced via this procedure are unique for every ZTF reference image (hereafter fcqf ID, following the nomenclature in Yao et al. (2019)). The ZTF field grid includes some overlap, and SNe that occur in overlap regions will have multiple fcqf IDs for a single filter. Estimates of the baseline flux (see Equation (1)) must account for the individual fcqf IDs.

The final photometric measurements in Yao et al. (2019) utilize estimates of the baseline flux, C, and χ^2_ν, which account for initially underestimated uncertainties, to correct the results of the forced PSF photometry. For this study, we do not employ the corrections suggested in Yao et al. (2019). Instead, we incorporate these values directly into our model so they can be marginalized over and effectively ignored.

3. A Search for Early Optical Flashes

We constrain the presence of extreme optical flashes in SNe Ia by searching our sample for sources with light curves that initially decline before following the typical rise of an SN Ia. While this simple criterion excludes events that exhibit an early bump, such as SNe 2017cbv and 2018oh, ZTF has found SNe Ia with an early optical flash (e.g., SN 2019yvq; see Miller et al. (2020)). Furthermore, the detection of bumps, as opposed to "flashes" where the flux is observed to decline, requires physical models of the early emission (e.g., Levanon & Soker 2017), and cannot be captured by the empirical power-law models used in this study. A comparison of the light curves to explosion models, as well as an estimate of the rate of potential flux excesses in the early light curves, will be presented in a future study (M. Deckers et al. 2020, in preparation).

Table 1
Upper Limits on the Rate of Optical Flashes in SNe Ia

			Flash Fraction	
$M_{\rm disk}$	$N_{\rm SN}$	$N_{\rm flash}$	C&P	Jeffreys
> -16.5 mag	33	0	<0.11	<0.07
> -16.0 mag	15	0	<0.22	<0.15
> -15.5 mag	8	0	<0.37	<0.26

Notes. $N_{\rm SN}$ is the number of SNe with an absolute magnitude at the epoch of discovery ($M_{\rm disk}$) fainter than the given cuts (-16.5, -16.0, -15.5 mag) in both the $g_{\rm ZTF}$ and $r_{\rm ZTF}$ bands. $N_{\rm flash}$ is the number of SNe with observed flashes. The flash fraction represents the 95% confidence interval upper limit on the rate of early flashes from SNe Ia. It has been calculated two ways: (i) using the method of Clopper & Pearson (1934), and (ii) using the Jeffreys prior (see Cai 2005).

Of the 127 SNe in our sample, only two (ZTF18abklljv and ZTF18abptsco) show a decline in flux following the epoch of discovery. When accounting for the uncertainties on the individual flux measurements, however, the observed decline in both ZTF18abklljv (SN 2018lpk) and ZTF18abptsco (AT 2018lpm) is statistically consistent with a constant flux during the first two nights of detection. We therefore conclude that an early optical flash is not detected in any of the SNe in our sample.

Despite this lack of detection, we can still constrain the rate of such events using binomial statistics. With no detections in 127 SNe, a naive estimate of the rate of optical flashes in SNe Ia is $\lesssim$3%. However, not every SN in our sample is discovered sufficiently early to rule out the presence of a flash. Using the distance moduli from Yao et al. (2019) and the host-galaxy reddening and Kcorrections from Bulla et al. (2020), we split our sample based on the absolute magnitude at the epoch of discovery, and use these subsets to constrain the rate of optical flashes in SNe Ia as summarized in Table 1.

With only eight SNe fainter than $M = -15.5$ mag at the epoch of discovery, we find a limit on faint optical flashes of $\lesssim$30%. Flashes this faint are expected when the SN ejecta collide with main-sequence companions (e.g., Kasen 2010). This limit is not that constraining, given that the companion-interaction signature is only expected in $\sim$10% of SNe (Kasen 2010).

4. Modeling the Early Rise of SNe Ia

Following arguments first laid out in Riess et al. (1999), the rest-frame optical flux of an SN Ia should evolve $\propto t^2$ shortly after explosion. For an ideal, expanding fireball, the observed flux through a passband covering the Rayleigh–Jeans tail of the approximately blackbody emission will be $f \propto R^2 T = v^2 t^2 T$, where f is the SN flux, T is the blackbody temperature, R is photospheric radius, v is the ejecta velocity, and t is the time since explosion.[17] While these idealized conditions are not

[17] All times reported in this study have been corrected to the SN rest frame.

perfectly met in nature, as T and v clearly change shortly after explosion (e.g., Parrent et al. 2012), their relative change is small compared to t. Thus, the "t^2law" should approximately hold, and indeed many studies of large samples of SNe Ia have shown that, in the blue optical filters, $f \propto t^2$ to within the uncertainties (e.g., Conley et al. 2006; Hayden et al. 2010; Ganeshalingam et al. 2011; González-Gaitán et al. 2012). At the same time, several recent studies of individual, low-redshift SNe Ia show strong evidence that a power-law model for the SN flux only reproduces the data if the power-law index, α, is significantly lower than 2 (e.g., Zheng et al. 2013, 2014; Shappee et al. 2016; Miller et al. 2018; Dimitriadis et al. 2019; Fausnaugh et al. 2019).

For this study, we characterize the early emission in a single filter from an SN Ia as a power law:

$$f_b(t) = C + H[t_{\rm fl}]A_b(t - t_{\rm fl})^{\alpha_b}, \qquad (1)$$

where $f_b(t)$ is the flux in filter b as a function of time t in the SN rest frame, C is a constant representing the baseline flux present in the reference image prior to SN discovery, $t_{\rm fl}$ is the time of first light,[18] $H[t_{\rm fl}]$ is the Heaviside function equal to 0 for $t < t_{\rm fl}$ and 1 for $t \geqslant t_{\rm fl}$, A_b is a constant of proportionality in filter b, and α_b is the power-law index describing the rise in filter b.

For ZTF, observations are obtained in the $g_{\rm ZTF}$ and $r_{\rm ZTF}$ bands, and we model the evolution in both filters simultaneously. While, strictly speaking, $t_{{\rm fl},g} \neq t_{{\rm fl},r}$, we expect these values to be nearly identical given the similarity of the SN ejecta opacity at these wavelengths (e.g., Figure 6 in Magee et al. 2018), and assume we cannot resolve the difference with ZTF data. Therefore, we adopt $t_{\rm fl}$ ($\approx t_{{\rm fl},g} \approx t_{{\rm fl},r}$) as a single parameter for our analysis. As discussed in Yao et al. (2019), C is a function of fcqf ID, which represents both the filter and ZTF field ID (see also Section 2).

Many of the SNe in our sample are observed at an extremely early phase in their evolution, at times when the spectral diversity in SNe Ia is not well-constrained; see, for example, the bottom panel of Figure 1 in Guy et al. (2007). As a result, we do not apply Kcorrections to the ZTF light curves prior to model fitting. Furthermore, without precise knowledge of the time of explosion, it is impossible to know which observations in the ZTF nightly sequence should be corrected and which should not. While examining SN 2011fe, Firth et al. (2015) find that ignoring Kcorrections leads to a systematic uncertainty on α of ± 0.1, which is smaller than the typical uncertainty we measure (see Section 5). This suggests that our inability to apply Kcorrections does not significantly affect our final conclusions.

If we assume that the observed deviations between the model flux and the data are the result of Gaussian scatter, the log-likelihood for the data is:

$$\ln \mathscr{L} \propto -\frac{1}{2}\sum_{d,i} \frac{[f_{d,i} - f_d(t_i)]^2}{(\beta_d \sigma_{d,i})^2} - \sum \ln(\beta_d \sigma_{d,i}), \qquad (2)$$

where the sum is over all fcqf IDs d and all observations i. Here, $f_{d,i}$ is the ith flux measurement with corresponding uncertainty $\sigma_{d,i}$, and β_d is a term we add to account for the fact that the uncertainties are underestimated (see Yao et al. 2019). Finally, $f_d(t_i)$ is the model, Equation (1) evaluated at the time of each observation t_i, with C replaced by C_d, the baseline for the individual fcqf IDs, and A_b and α_b replaced by $A_{b|d}$ and $\alpha_{b|d}$, respectively, as these terms depend on fcqf ID, but only the filter b and not the field ID.

[18] Note that $t_{\rm fl}$ is not the time of explosion, but rather the time when optical emission begins for the SN, as the observed emission due to radioactive decay in the interior of the SN ejecta must first diffuse through the photosphere; see, e.g., Piro & Nakar (2013, 2014).

Table 2
Model Parameters θ and Their Priors

θ	Description	Prior
C_d	Baseline flux per fcqf ID d	$\mathcal{U}(-10^8, 10^8)$
$t_{\rm fl}$	Time of first light	$\mathcal{U}(-100, 0)$
$A'_{b\|d}$	Proportionality factor per filter b	$A'^{-1}_{b\|d}10^{-\alpha_{b\|d}}$
$\alpha_{b\|d}$	Rising power-law index per filter b	$\mathcal{U}(0, 10^8)$
β_d	Uncertainty scale factor per fcqf ID d	β_d^{-1}

Note. The factor of $10^{-\alpha_{b|d}}$ in the prior for $A'_{b|d}$ follows from the change of variables (see Appendix A).

Ultimately, we only care about three model parameters: $t_{\rm fl}$, and the power-law index describing the rise in the $g_{\rm ZTF}$ and $r_{\rm ZTF}$ filters, hereafter α_g and α_r, respectively. Following Bayes' Law, we multiply the likelihood by a prior and use an affine-invariant, ensemble Markov Chain Monte Carlo (MCMC) technique (Goodman & Weare 2010) to approximate the model posterior.

There is a strong degeneracy between $A_{b|d}$ and $\alpha_{b|d}$, which we find can be removed with the following change of variables $A'_{b|d} = A_{b|d}10^{\alpha_{b|d}}$ in Equation (1). We adopt the Jeffreys prior (Jeffreys 1946) for the scale parameters $A_{b|d}$ and β_d, and wide flat priors for all other model parameters, as summarized in Table 2. The MCMC integration is performed using `emcee` (Foreman-Mackey et al. 2013). Within the ensemble, we use 100 walkers, each of which is run until convergence or three million steps, whichever comes first. We test for convergence by examining the average autocorrelation length of the individual chains τ after every 20,000 steps. We consider the chains converged if $n_{\rm steps} > 100\tau$, where $n_{\rm steps}$ is the total number of steps in each chain, and the change in τ relative to the previous estimate has changed by $<1\%$.

A key decision in modeling the early evolution of SNe Ia light curves is deciding what is meant by "early." While the simplistic power-law models adopted here and elsewhere can describe the flux of SNe Ia shortly after explosion, it is obvious that these models cannot explain the full evolution of SNe Ia, as they never turn over and decay. Throughout the literature, there are various definitions of early, ranging from some studies defining early relative to the amount of time that has passed following the epoch of discovery (e.g., Nugent et al. 2011; Zheng et al. 2013; Miller et al. 2018) to others defining it relative to the time of B-band maximum (e.g., Riess et al. 1999; Aldering et al. 2000; Conley et al. 2006; Dimitriadis et al. 2019), while others define early in terms of the fractional flux relative to maximum light (e.g., Firth et al. 2015; Olling et al. 2015; Fausnaugh et al. 2019). Here, we adopt the latter definition in order to be consistent with recent work using extremely high-cadence, high-precision light curves from the space-based Kepler K2 (Howell et al. 2014) and the Transiting Exoplanet Survey Satellite (Ricker et al. 2015) missions (e.g., Olling et al. 2015; Fausnaugh et al. 2019). As in Olling et al. (2015), we only include observations up to 40% of the peak amplitude of the SN.[19] We find that this particular choice, 40% instead of 30% or 50%, does slightly affect the final inference for the model parameters (see Appendix D for further details).

Of the 127 SNe Ia in our sample, we find that the MCMC chains converge for every SNe but one, ZTF18aaqnrum (SN 2018bhs). Nevertheless, we retain it in our sample as $n_{\rm steps} \approx 81\,\tau$ after three million steps, suggesting several independent samples within the chains (this SN is later excluded from the sample; see Appendix B).

Example corner plots illustrating good, typical, and poor constraints on the model parameters, $t_{\rm fl}$, α_g, and α_r, are shown in Figures 1–3, respectively. In this context, good, typical, and poor are defined relative to the width of the 90% credible region for $t_{\rm fl}$ (CR_{90}). Roughly speaking, the good models have $\mathrm{CR}_{90} \lesssim 1.5$ days (∼34 SNe), the median models have $\mathrm{CR}_{90} \approx 2.5$ days (∼61 SNe), and the poor models have $\mathrm{CR}_{90} \gtrsim 4$ days (∼32 SNe). From the corner plots, it is clear that there is a positive correlation between α_g and α_r, which makes sense given the relatively similar regions of the spectral energy distribution (SED) traced by these filters. Finally, $t_{\rm fl}$ exhibits significant covariance with each of the α parameters. While we report marginalized credible regions on all model parameters in Table 3, the full posterior samples should be used for any analysis utilizing the results of our model fitting (see, e.g., Bulla et al. 2020).

The bottom panels of Figures 1–3 display the light curves for the corresponding corner plots shown in the top panels. In addition to the observations, we also show multiple models based on random draws from the posterior, and the residuals normalized by the observational uncertainties (pull) relative to the maximum *a posteriori* estimate from the MCMC sampling. As illustrated in Figure 1, we can place tight constraints on the model parameters for light curves with a high S/N. These SNe are typically found at low redshift, and are monitored with good sampling and at high photometric precision. As expected, as the S/N decreases (Figure 2) or the typical interval between observations increases (Figure 3), it becomes more and more difficult to place meaningful constraints on $t_{\rm fl}$ or α. We visually examine posterior models for each light curve and flag those that produce unreliable parameter constraints. We use this subset of sources to identify SNe that should be excluded from the full sample analysis described in Section 5 below (see Appendix B). These flagged sources are noted in Table 3.

5. The Mean Rise Time and Power-law Index for SNe Ia

Below, we examine the results from our model fitting procedure to investigate several photometric properties of *normal* SNe Ia. We define normal via the spectroscopic classifications presented in Yao et al. (2019). SNe classified as SN 1986G-like, SN 2002cx-like, Ia-CSM, and super-Chandrasekhar explosions are excluded from the analysis below. These seven peculiar events are discussed in detail in Appendix C. The remaining 120 normal SNe Ia in our sample have $-2 \lesssim x_1 \lesssim 2$, where x_1 is the `SALT2` shape parameter, which is well within the range of SNe that are typically used for cosmography (e.g., Scolnic et al. 2018). Estimates of $t_{\rm rise}$ and α for all SNe in our sample, including the seven peculiar SNe Ia discussed in Appendix C, are presented in Table 3.

5.1. Mean Rise Time of SNe Ia

From the marginalized 1D posteriors for $t_{\rm fl}$, we can examine the typical rise time for SNe Ia. The model given in Equation (1) constrains $t_{\rm fl}$, yet what we ultimately care about is the rise time, $t_{\rm rise}$. We measure $t_{\rm fl}$ relative to $T_{B,\rm max}$, which itself has some uncertainty.[20] An estimate of $t_{\rm rise}$ must therefore account for the uncertainties on both $t_{\rm fl}$ and $T_{B,\rm max}$. Aldering et al. (2000) critically showed that ignoring the uncertainties on the time of maximum could lead to $t_{\rm rise}$ estimates that are incorrect by $\gtrsim$2 days.

To measure $t_{\rm rise}$, we use a Gaussian kernel density estimation (KDE) to approximate the 1D marginalized probability density function (PDF) for $t_{\rm fl}$. The width of the kernel is determined via cross-validation and the KDE is implemented with `scikit-learn` (Pedregosa et al. 2011). The PDF is multiplied by -1 and convolved with a Gaussian with the same variance as the uncertainties on $T_{B,\rm max}$ in order to determine the final PDF for $t_{\rm rise}$. The cumulative density function of this PDF is used to determine the median and 90% credible region on $t_{\rm rise}$. We assume there is no significant covariance in the uncertainties on $t_{\rm fl}$ and $T_{B,\rm max}$. These times are estimated using independent methods and portions of the light curve, which is why we can convolve the uncertainties in making the final estimation of $t_{\rm rise}$.

In Figure 4, we show the PDF for $t_{\rm rise}$ for the 120 normal SNe in our sample. We highlight three subsets of the normal SNe in Figure 4: SNe with reliable model parameters (see Appendix B) and known host-galaxy redshifts (hereafter the reliable-$z_{\rm host}$ group), SNe with reliable model parameters and unknown host-galaxy redshifts (hereafter the reliable-$z_{\rm SN}$ group; the reliable-$z_{\rm host}$ and reliable-$z_{\rm SN}$ groups together form the reliable group), and SNe with large uncertainties in the model parameters, typically due to sparse sampling around $t_{\rm fl}$ or low photometric precision (hereafter the unreliable group).

Figure 4 shows that $t_{\rm rise}$ is typically several days shorter for SNe in the unreliable group relative to SNe in the reliable group. This provides another indication that the low-quality light curves in our sample are insufficient for constraining the model parameters. Figure 4 also reveals that the rise time among individual SNe does not tend toward a common mean value. If all SNe Ia could be described with a single rise time, we could estimate that mean value by multiplying the individual PDFs in Figure 4 together. This product provides no support for a single rise time to describe all SNe Ia (i.e., it is effectively equal to zero everywhere).

As a population, SNe Ia have a mean $t_{\rm rise} \approx 17.9$ days, where we have estimated this value by taking a weighted mean of the median value of the $t_{\rm rise}$ PDFs, with weights equal to the square of the inverse of the 68% credible region. The mean $t_{\rm rise}$ increases to ≈18.5 and 18.7 days when considering only the

[19] We do this separately in the $g_{\rm ZTF}$ and $r_{\rm ZTF}$ filters. In practice, we subtract a preliminary estimate of the flux baseline derived from the median flux value for all observations that occurred >20 days (in the SN rest frame) before $T_{B,\rm max}$. We then divide all flux values by the peak flux determined in Yao et al. (2019). Finally, we calculate the inverse-variance weighted mean flux for every night of observations, and only retain those nights with $f_{\rm mean} \leqslant 0.4 f_{\rm max}$ for model fitting.

[20] In this study, $t_{\rm rise}$ represents the rise time to B-band maximum, as we measure time relative to $T_{B,\rm max}$ and assume $t_{\rm fl}$ is the same in the B, $g_{\rm ZTF}$, and $r_{\rm ZTF}$ filters. This assumption is reasonable given that the opacities in an SN photosphere at frequencies $\lesssim 10^{15}$ Hz ($\gtrsim$3000 Å) are dominated by Thomson scattering (see Figure 6 in Magee et al. 2018). Furthermore, the significant overlap between the B and $g_{\rm ZTF}$bands suggests that $t_{\rm fl}$ should be extremely similar, if not identical, in these two filters.

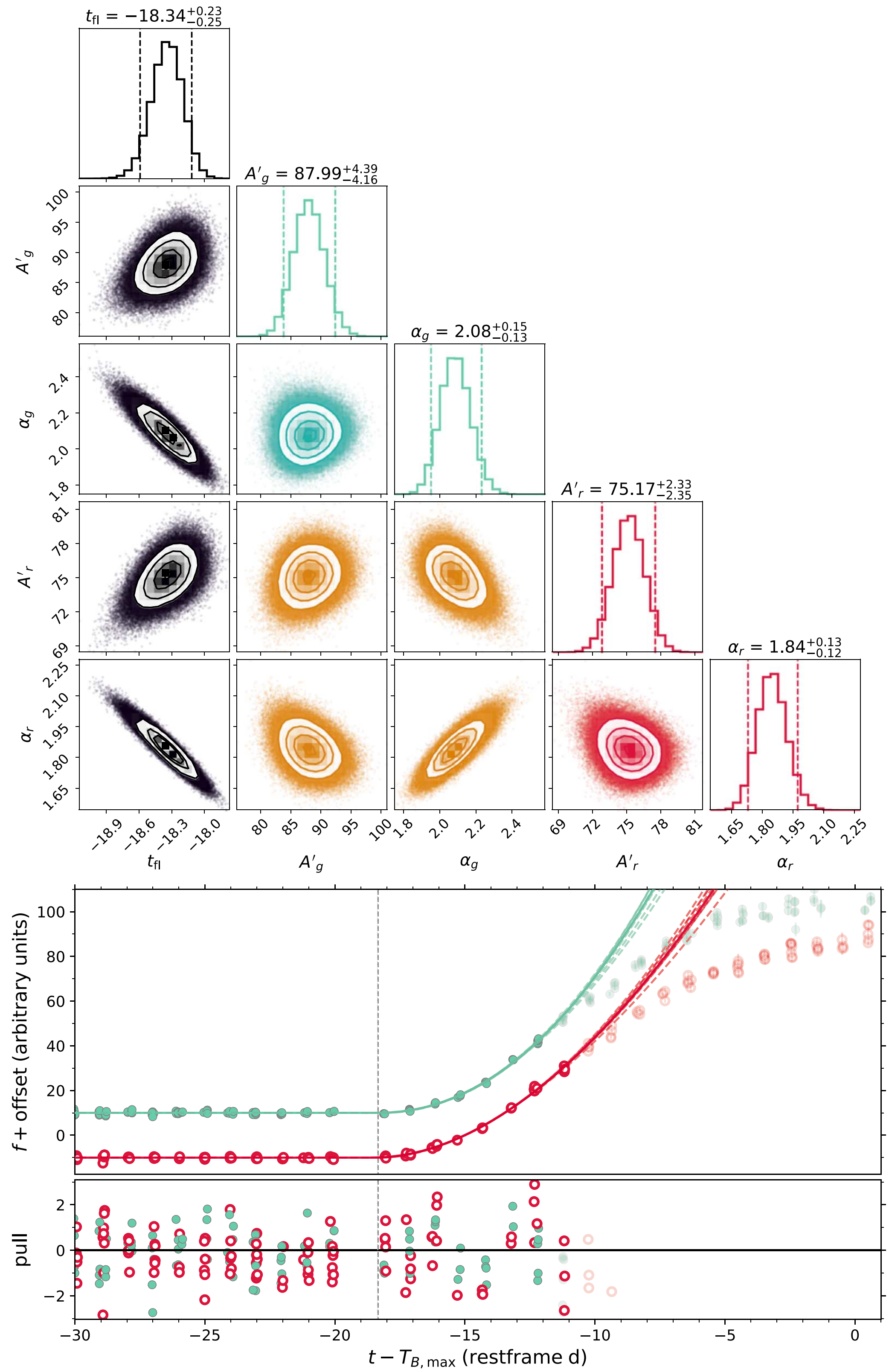

Figure 1. *Top*: Corner plot showing the posterior constraints on $t_{\rm fl}$, α_g, α_r, and the respective constants of proportionality, A'_g and A'_r for ZTF18abgmcmv (SN 2018eay). ZTF18abgmcmv is well-fit by the model. For clarity, the C_d and β_d terms are excluded (in general, they do not exhibit strong covariance with the parameters shown here, as they are tightly constrained by the pre-SN observations). Marginalized one-dimensional distributions are shown along the diagonal, along with the median estimate and the 90% credible region (shown with vertical dashed lines). *Bottom*: ZTF light curve for ZTF18abgmcmv showing the $g_{\rm ZTF}$ (filled, green circles) and $r_{\rm ZTF}$ (open, red circles) evolution of the SN in the month prior to $T_{B,\rm max}$. Observations included in the model fitting (i.e., those with $f \leqslant 0.4 f_{\rm max}$) are dark and solid, while those that are not included are faint and semi-transparent. The maximum *a posteriori* model is shown via a thick solid line, while random draws from the posterior are shown with semi-transparent dashed lines. The vertical dashed line shows the median 1D marginalized posterior value of $t_{\rm fl}$, while the thin, light gray vertical line shows $t_{\rm fl}$ for the maximum *a posteriori* model (these values are nearly identical for this SN, and the thin gray line is not visible). The bottom panel shows the residuals relative to the maximum *a posteriori*model normalized by the observational uncertainties (pull), where the factor β_d has been included in the calculation of the pull.

reliable and reliable-z_{host} subsamples, respectively (see Table 4). The scatter, estimated via the sample standard deviation, about these mean values is ∼1.8 days.

5.2. Mean Power-law Index of the Early Rise

We use a similar procedure to report the PDF of α_g and α_r under the assumption of a flat prior. The posterior samples for α shown in Figures 1–3 include a factor of $10^{-\alpha}$ following the change of variables from A to A' (see Table 2 and Appendix B). To remove this factor, we estimate the 1D marginalized PDF of α using a KDE as above. This PDF is next divided by $10^{-\alpha}$, and then renormalized to integrate to 1 on the interval from 0 to 10. This final normalized PDF provides an estimate of α_g and α_r assuming a $\mathcal{U}(0, 10)$ prior.

The PDFs for α_g for normal SNe Ia are shown in Figure 5. The most precise estimates of α_g come from the reliable-z_{host} group, which are clustered around $\alpha_g \approx 2$. There are, however, individual reliable-z_{host} SNe that provide support for α_g as low as ∼0.7 and as high as ∼3.5, meaning α_g can take on a wide range of values.

The weighted sample mean is $\alpha_g \approx 1.9$ for normal SNe Ia in the ZTF sample. This value increases to ∼2.1 when reducing the sample to the reliable group or the reliable-z_{host} group. The population scatter is ∼0.6 (see Table 4). For α_r, the weighted sample mean is ∼1.7, ∼1.9, and ∼2.0 for the full sample, the reliable group, and reliable-z_{host} group, respectively. The typical scatter in α_r is 0.5 (see Table 4). As noted in Section 6.1, there is a tight correlation between α_g and α_r, and thus we do not show the individual PDFs for α_r.

In both the g_{ZTF} and r_{ZTF} filters, the mean rising power-law index for the initial evolution of the SN is close to 2, as might be expected in the expanding fireball model. While the mean value of α is ∼2, it is noteworthy that several SNe in the reliable-z_{host} sample are clearly not consistent with $\alpha = 2$. If we multiply the individual PDFs of α_g or α_r together, we find there is no support for a single mean value of α for all SNe Ia. This suggests that models using a fixed value of α are insufficient to explain the general population of normal SNe Ia (though see also Section 7).

5.3. Mean Color Evolution

Here, we examine the mean initial color evolution of SNe Ia, under the assumption that the early emission from SNe Ia can correctly be described by the power-law model adopted in Section 4. This analysis does not address the initial colors of SNe Ia; for a more detailed analysis of the initial colors and color evolution of SNe Ia, see Paper III in this series (Bulla et al. 2020).

Unlike t_{rise} and α, we do find evidence for a single mean value of the early color evolution of SNe Ia, as traced by $\alpha_r - \alpha_g$. If the early evolution in the g_{ZTF} and r_{ZTF} filters is a power law in time, then the $g_{ZTF} - r_{ZTF}$ color, in mag, will be proportional to $(\alpha_r - \alpha_g)\log_{10}(t - t_{fl})$.

To estimate $\alpha_r - \alpha_g$, we use a similar procedure as above; however, we need to estimate the marginalized joint posterior on α_g and α_r, $\pi(\alpha_g, \alpha_r | t_{fl}, A_b', \beta_d)$ in order to correct the posterior estimates for the priors on α. We estimate the 2D joint posterior via a Gaussian KDE, correct this distribution for the priors on α_g and α_r, and then obtain random draws from this distribution to estimate the 1D marginalized likelihood estimates on $\alpha_r - \alpha_g$. The PDFs for $\alpha_r - \alpha_g$ for individual SNe are shown in Figure 6.

Unlike the estimates for t_{rise} and α alone, $\alpha_r - \alpha_g$ is clearly clustered around ∼−0.2 for the reliable group. Multiplying the likelihoods of the reliable-z_{host} group together produces support for a single mean value of $\alpha_r - \alpha_g = -0.175^{+0.016}_{-0.015}$, where the uncertainties on that estimate represent the 90% credible region. The mean PDF for the reliable-z_{host} group is shown as the thick, solid black line in Figure 6. A mean value of $\alpha_r - \alpha_g$ suggests that a typical, normal SN Ia becomes bluer in the days after explosion. Such an evolution makes sense for an optically thick, radioactively heated, expanding ejecta (e.g., Piro & Morozova 2016; Magee et al. 2020). There are, however, clear examples of individual SNe that do not exhibit this behavior, e.g., SN 2017cbv (Hosseinzadeh et al. 2017) and iPTF 16abc (Miller et al. 2018), meaning this mean behavior is not prescriptive for every SN Ia. These results exclude SNe from the unreliable group, and their inclusion would remove any support for a single mean value of $\alpha_r - \alpha_g$. This is largely due to a small handful of events that feature extreme values of $\alpha_r - \alpha_g$ because there are gaps in the observational coverage of one of the two filters (see the upper right panel of Figure 7).

6. Population Correlations

In addition to looking at the typical values of t_{rise} and α for SNe Ia, we also examine the correlations between these parameters, as well as how they evolve with redshift, z. These correlations may reveal details about the explosion physics of SNe Ia; for example, if strong mixing in the SN ejecta affects the early evolution, as found in Piro & Morozova (2016), Magee et al. (2018), and Magee et al. (2020), then any correlations with α may be related to ejecta mixing. If the model parameters are correlated with redshift, that could be evidence for either the cosmic evolution of SNe Ia progenitors or inadequacies in the model.

The correlation between t_{rise}, α_g, α_r, and z is shown in Figure 7. We do not show the correlation between α_r and z or between α_g and t_{rise}, as this information is effectively redundant given the tight correlation between α_g and α_r (top right panel of Figure 7).

6.1. Correlation between α_g and α_r

The most striking feature in Figure 7 is the tight correlation between α_g and α_r. This result is reasonable because the SN SED is approximately a blackbody, and the g_{ZTF} and r_{ZTF} filters are relatively line-free (compared to the UV) and sample adjacent portions of the Rayleigh–Jeans tail. Thus, the evolution should be nearly identical in the two filters. SNe with reliable model parameters follow a tight locus around $\alpha_r - \alpha_g \approx -0.2$, with the only major outliers from this relation being SNe in the unreliable group.

The Spearman rank-ordered correlation coefficient for α_g and α_r is highly significant for the entire population ($\rho > 0.5$). Restricting the sample to SNe with reliable model parameters increases the significance of the correlation dramatically ($\rho > 0.9$). Thus, knowledge of the power-law index in either filter provides a strong predictor for the power-law index in the other filter.

Table 3
Ninety Percent Credible Regions for Marginalized Model Parameters (Uninformative Prior)

ZTF Name	TNS Name	z[a]	$t_{\rm rise}$(day)			α_g			α_r			$\alpha_r - \alpha_g$			Reliable[b]	Normal[c]
			5	50	95	5	50	95	5	50	95	5	50	95		
ZTF18aailmnv	SN 2018ebo	0.080	14.23	14.91	16.29	0.69	1.05	1.81	0.41	0.74	1.36	−0.86	−0.34	0.09	n	y
ZTF18aansqun	SN 2018dyp	0.0597	12.45	13.69	16.33	1.15	3.24	5.66	0.23	0.73	1.88	−3.06	−2.81	−1.46	n	y
ZTF18aaoxryq	SN 2018ert	0.0940	13.30	14.06	15.42	0.31	0.64	1.10	0.14	0.41	0.84	−0.65	−0.22	0.20	n	y
ZTF18aapqwyv	SN 2018bhc	0.0560	14.02	15.07	17.05	1.61	2.55	4.28	0.54	1.52	3.31	−1.98	−0.97	0.03	n	y
ZTF18aapsedq	SN 2018bgs	0.0720	17.56	18.54	19.73	1.62	2.05	2.62	1.61	3.20	5.79	−0.00	1.47	3.18	n	y
ZTF18aaqcozd	SN 2018bjc	0.0732	10.85	12.13	16.53	0.56	2.28	4.61	1.13	3.47	5.46	0.63	0.81	0.99	n	y
ZTF18aaqcqkv	SN 2018lpc	0.1174	13.16	14.79	15.99	0.62	2.51	5.21	0.21	1.64	3.69	−1.74	0.80	1.82	n	y
ZTF18aaqcqvr	SN 2018bvg	0.0716	13.69	14.32	15.62	0.41	0.69	1.32	0.52	0.89	1.73	0.00	0.25	0.52	n	y
ZTF18aaqcugm	SN 2018bhi	0.0619	13.79	15.10	17.06	1.23	2.00	3.00	1.01	1.65	2.49	−0.74	−0.33	0.02	n	y
ZTF18aaqffyp	SN 2018bhr	0.070	11.76	16.21	19.98	0.03	0.31	1.35	0.02	0.23	1.10	−1.15	−0.06	0.83	n	y
ZTF18aaqnrum	SN 2018bhs	0.066	11.64	14.52	17.75	0.14	1.64	2.97	0.36	2.88	4.59	−2.20	0.53	2.68	n	y
ZTF18aaqqoqs	SN 2018cbh	0.082	18.31	18.85	19.67	1.08	1.33	1.72	1.06	1.39	1.88	−0.17	0.06	0.33	y	y
ZTF18aarldnh	SN 2018lpd	0.1077	14.07	15.14	17.17	1.20	2.22	4.21	0.77	1.33	2.37	−1.71	−1.20	−0.37	n	y
ZTF18aarqnje	SN 2018bvd	0.117	14.65	16.55	18.23	1.27	1.97	3.24	0.63	1.36	2.62	−1.53	−0.62	0.27	n	y
ZTF18aasdted	SN 2018big	0.0181	18.76	18.91	19.08	1.46	1.54	1.63	1.30	1.39	1.50	−0.21	−0.15	−0.09	y	y

Notes. The table includes the 5th, 50th, and 95th percentiles for the four parameters of interest: $t_{\rm rise}$, α_g, α_r, $\alpha_r - \alpha_g$. The 90% credible regions are obtained by subtracting the 5th percentile from the 95th percentile. Estimates for $t_{\rm rise}$ come from $t_{\rm fl}$ while accounting for the uncertainties on $t_{B,\rm max}$, while estimates for the α parameters have been corrected to a flat prior (see text for further details).

[a] Redshifts are reported to four decimal places, if the SN host galaxy redshift ($z_{\rm host}$) is known. Otherwise, the SN redshift ($z_{\rm SN}$) is reported to three decimal places; see Yao et al. (2019) for further details.

[b] Flag for SNe with reliable model parameters (see Appendix B): y = reliable group, and n = unreliable group (see text).

[c] Flag for normal SNe Ia: y = normal, n = peculiar (the seven peculiar SNe Ia in our sample are discussed in Appendix C; their rise times are measured relative to $T_{g,\rm max}$).

(This table is available in its entirety in machine-readable form.)

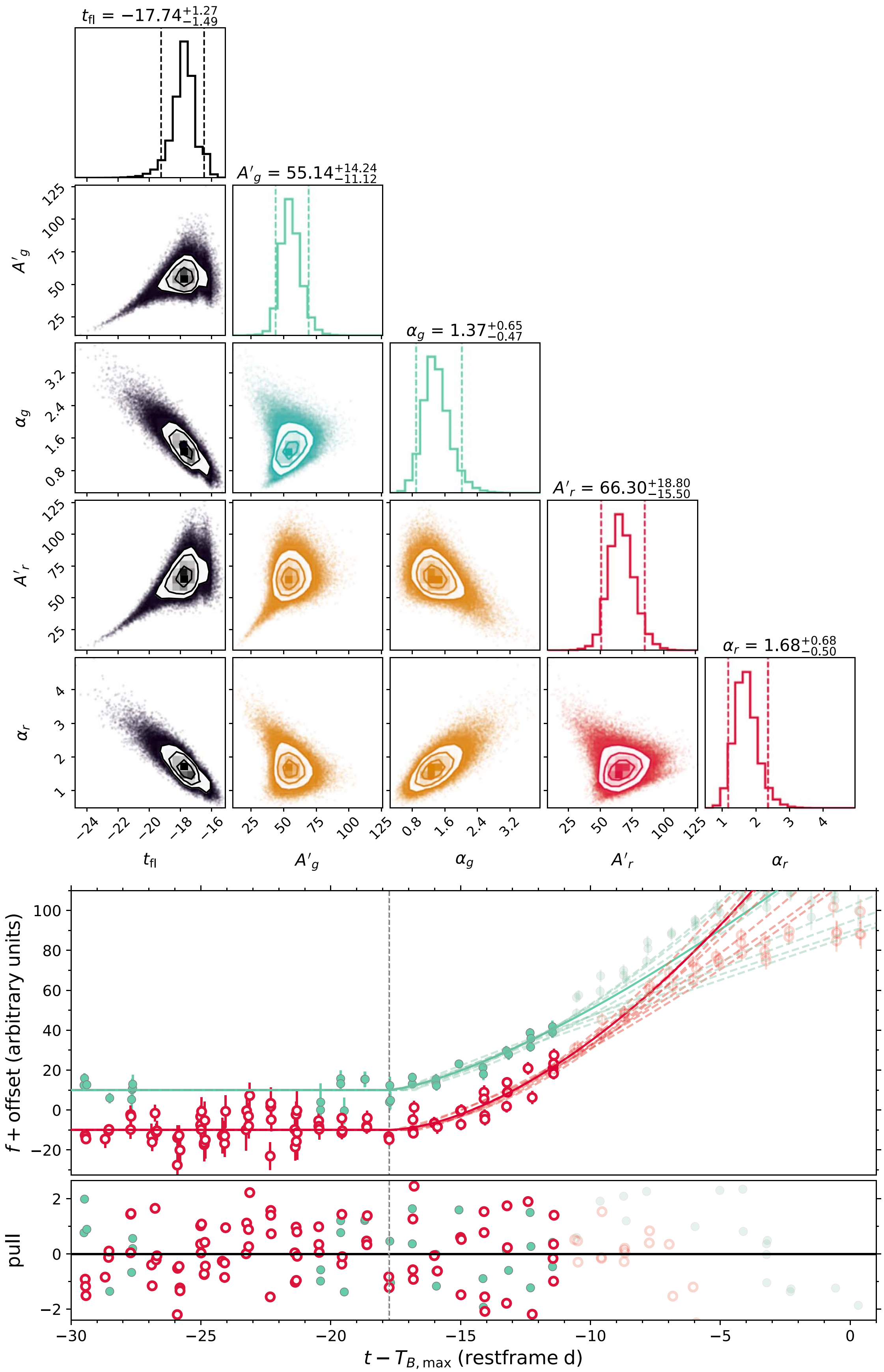

Figure 2. Same as Figure 1 for ZTF18abukmty (SN 2018lpz), a typical SN in our sample. For ZTF18abukmty, the median 1D marginalized posterior value of t_{fl} and the maximum *a posteriori* value of t_{fl} are nearly identical, so the thin gray line showing the latter is not visible.

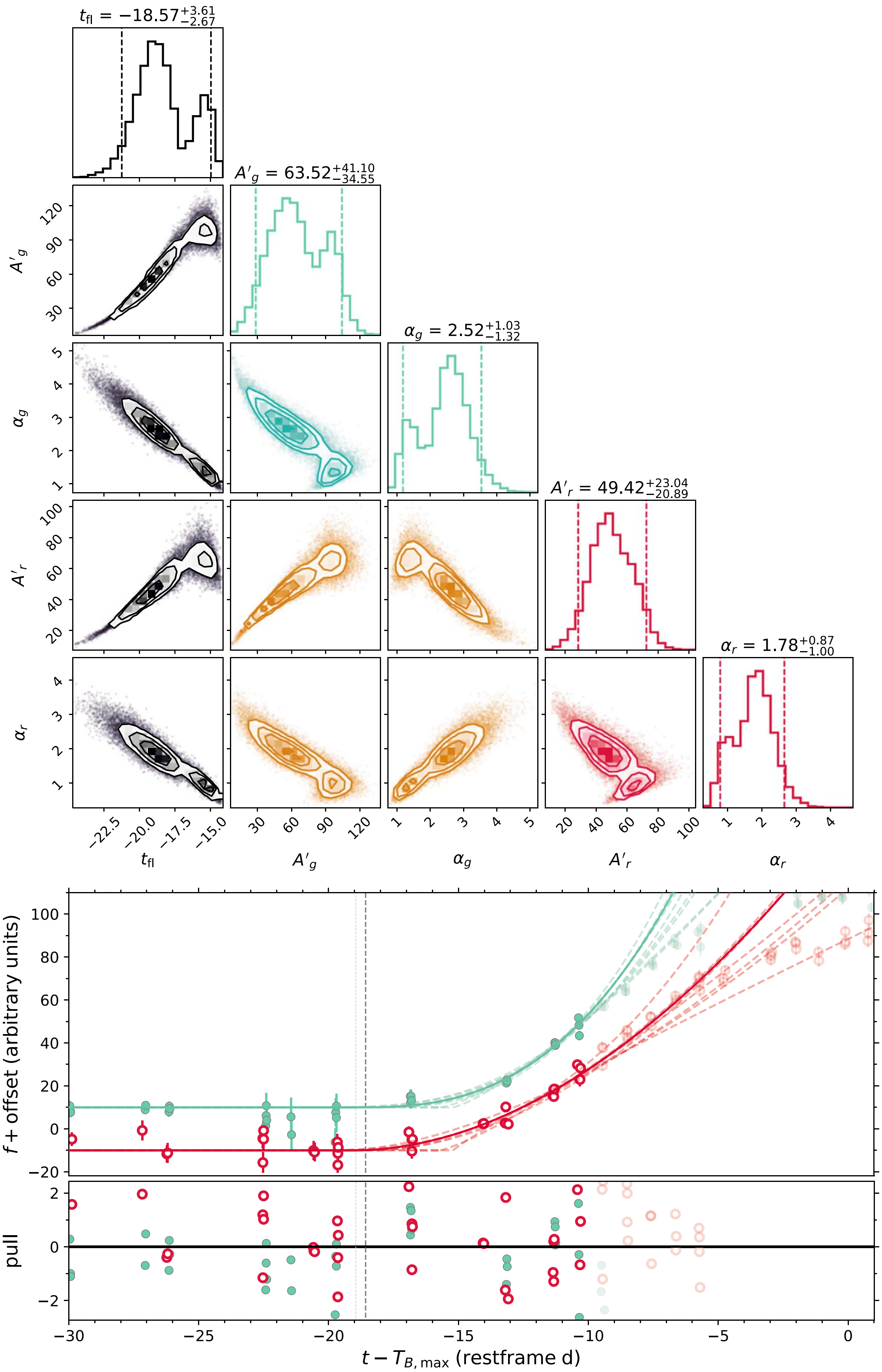

Figure 3. Same as Figure 1 for ZTF18aazabmh (SN 2018crr), an SN that does not significantly constrain the model parameters.

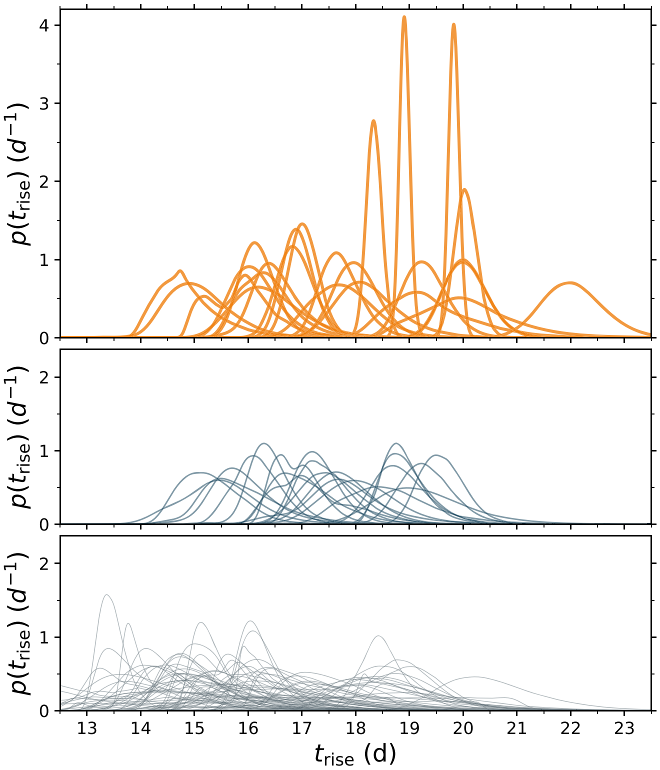

Figure 4. Marginalized posterior distribution of the rise time $t_{\rm rise}$ for normal SNe Ia in our sample. The sample has been divided into three groups (as described Appendix B): thick orange lines show SNe from the reliable-$z_{\rm host}$ group (top panel), dark blue lines show SNe from the reliable-$z_{\rm SN}$ group (middle panel), and thin gray lines show SNe from the unreliable group (bottom panel). From the individual PDFs, it is clear that there is no support for a single mean $t_{\rm rise}$ to describe every SN in the sample.

6.2. Correlations with Redshift—Systematics, Not Cosmic Evolution

While less prominent, Figure 7 additionally shows that both $t_{\rm rise}$ and α are correlated with redshift. This result is somewhat surprising: naively, it suggests some form of cosmic evolution in SNe Ia, with SNe at $z \approx 0.08$ having rise times that are several days shorter than SNe at $z \approx 0.02$. The small range of redshifts in our sample, as well as those in several previous studies (e.g., Aldering et al. 2000; Conley et al. 2006; González-Gaitán et al. 2012; Jones et al. 2019), place this naive explanation in doubt. Instead, these correlations are the result of building a sample from a flux-limited survey.

Given that ZTF cannot detect SNe when their observed brightness is $g_{\rm ZTF} \gtrsim 21.5$ mag (Bellm et al. 2019b; Masci et al. 2019), SNe at progressively higher redshifts are discovered at a later phase in their evolution. The large degeneracies in the model presented in Equation (1), namely between $t_{\rm fl}$, A, and α, allow for a great deal of flexibility when fitting the data. For SNe discovered at later phases, it is possible to adjust $t_{\rm fl}$ while decreasing A and α, such that $t_{\rm fl}$ occurs around the epoch of first detection (resulting in a shorter rise time).

We illustrate this effect in Figure 8, which shows that the inferred rise time for identical SNe decreases as those SNe are observed at successively higher redshifts. We use the four normal SNe with $z \leqslant 0.03$ and simulate their appearance at higher redshift by making the (oversimplified) assumption that all detections are in the sky-background-dominated regime. Thus, in any given epoch the S/N $\propto d_L^{-2}$, where d_L is the SN luminosity distance. To simulate the SN at some new redshift, $z_{\rm sim}$, we multiply the uncertainties by $(d_{L,{\rm sim}}/d_{L,{\rm obs}})^2$, where $d_{L,{\rm sim}}$ is the luminosity distance at $z_{\rm sim}$, and $d_{L,{\rm obs}}$ is the observed luminosity distance to the SN.[21] Using these increased uncertainties, we randomly resample the observed flux values from a normal distribution with mean equal to the original flux and variance equal to the square of the distance-scaled uncertainty. After correcting the observation times to the simulated rest frame, we fit the noisier simulated data with the procedure from Section 4. We simulate the appearance of these SNe at redshifts $z = 0.05$, 0.075, 0.1, and 0.15. Only the models that converge are shown in Figure 8.

The results shown in Figure 8 are clear: SNe discovered at higher redshifts have systematically smaller estimates for $t_{\rm rise}$. This result is simple to understand, as higher-redshift SNe will not be detected until later in their evolution. A stronger prior on any of the model parameters would help to combat this effect (see Section 7), though we avoid strong priors, as previously discussed, due to the wide range of α and $t_{\rm fl}$ that has been reported in the literature.

This effect also explains the correlation seen in the bottom right panel of Figure 7. SNe detected later in their evolution will be evolving less rapidly as the rate of change in brightness continually decreases until the time of maximum light. Hence, a later detection provides a lower value of α. Indeed, a recreation of Figure 8 showing α_g instead of $t_{\rm rise}$ shows α_g decreasing with increasing redshift. Thus, the observed correlations with redshift seen in Figure 7 can be entirely understood as the result of ZTF being a flux-limited survey.

The implications of this result have consequences well beyond the ZTF sample discussed here. Essentially all SN surveys are flux-limited, meaning the systematics associated with redshift will affect any efforts to determine $t_{\rm rise}$ or α in those data as well. The inclusion of higher-redshift SNe in the sample will, on average, bias estimates of $t_{\rm rise}$ and α to lower values. Even more concerning is the possibility that this trend may continue to very low redshifts ($z \ll 0.01$). The paucity of SNe in this redshift range, due to the relatively small volume probed, make it difficult to test for such an effect. Due to the systematic identified here, it may be the case that the rise time (and by extension, also α) is underestimated for every SN in the literature. Detailed simulations with realistic SN light curves are needed to test this possibility.

6.3. Correlation between t_{rise} and α

The lower right panel of Figure 7 shows that $t_{\rm rise}$ and α_r are correlated (and by extension, $t_{\rm rise}$ and α_g are also correlated). The Spearman correlation coefficient for $t_{\rm rise}$ and α_r is significant ($\rho \gtrsim 0.5$) for both the entire population of SNe in this study and the reliable subset as well. Similar values are found for $t_{\rm rise}$ and α_g. The positive correlation between $t_{\rm rise}$ and α is also found in González-Gaitán et al. (2012).

The origins of such a correlation may be a consequence of the ^{56}Ni distribution in the SN ejecta. In Magee et al. (2020), a suite of models is developed to explore the effects of ^{56}Ni mixing on the resulting emission from SNe Ia. The full family of models in Magee et al. (2020), which was designed to cover a wide range of parameter space and not the physical space occupied by observed SNe Ia, does not show significant

[21] Following Yao et al. (2019), we adopt a flat ΛCDM cosmology with $H_0 = 73.24$ km s^{-1} Mpc^{-1} (Riess et al. 2016) and $\Omega_m = 0.275$ (Amanullah et al. 2010) to calculate d_L for the SNe.

Table 4
Population Mean and Scatter For t_{rise} and α

	Uninformative Prior									$\alpha = 2$ Prior		
Subset	N	t_{rise} (day)	$\sigma_{t_{rise}}$ (day)	α_g	σ_{α_g}	α_r	σ_{α_r}	$\alpha_r - \alpha_g$	$\sigma_{\alpha_r - \alpha_g}$	N	t_{rise} (day)	$\sigma_{t_{rise}}$ (day)
Normal	120	17.92 ± 0.04	1.81	1.89 ± 0.02	0.75	1.73 ± 0.02	0.80	−0.18 ± 0.01	0.73	120	21.59 ± 0.02	1.89
Reliable	47	18.53 ± 0.05	1.62	2.05 ± 0.02	0.53	1.89 ± 0.02	0.50	−0.17 ± 0.01	0.23	115	21.59 ± 0.02	1.90
Reliable-z_{host}	25	18.73 ± 0.05	1.85	2.12 ± 0.02	0.59	1.99 ± 0.03	0.54	−0.18 ± 0.02	0.17	58	21.54 ± 0.02	2.09
Volume-limited ($z < 0.06$) subset												
Normal	28	18.61 ± 0.05	2.26	2.05 ± 0.03	0.76	1.95 ± 0.03	0.67	−0.21 ± 0.01	0.86	28	21.68 ± 0.02	1.53
Reliable	16	18.91 ± 0.05	1.75	2.13 ± 0.03	0.54	2.01 ± 0.03	0.52	−0.18 ± 0.02	0.08	27	21.68 ± 0.02	1.51
Reliable-z_{host}	15	18.95 ± 0.05	1.71	2.14 ± 0.03	0.51	2.02 ± 0.03	0.50	−0.18 ± 0.02	0.09	24	21.67 ± 0.02	1.56
DIC preferred		…	…	…	…	…	…	…	…	28	19.87 ± 0.03	1.46
DIC–uninformative	9	19.20 ± 0.06	1.38	2.14 ± 0.03	0.55	2.02 ± 0.03	0.52	−0.19 ± 0.02	0.08	…	…	…

Notes. Table includes the weighted mean (see text), plus standard uncertainty in the weighted mean, as well as the scatter (the sample standard deviation), for the four parameters of interest, t_{rise}, α_g, α_r, $\alpha_r - \alpha_g$, for the uninformative and $\alpha = 2$ priors. N is the number of SNe in each subset of the data, which are defined as follows (see text for more detailed definitions): normal—normal SNe Ia; reliable—SNe with reliable model parameters; reliable-z_{host}—reliable SNe with known host galaxy redshifts; DIC preferred—results from the $\alpha = 2$ prior, *unless the DIC prefers the uninformative prior* (see Section 7.2; only applies to t_{rise}); DIC–uninformative—only SNe where the DIC prefers the uninformative prior (see Section 7.2; excludes the $\alpha = 2$ prior by construction). The volume-limited subset includes only SNe with $z < 0.06$ (see Section 8). Note that the definition of reliable differs for the uninformative and $\alpha = 2$ priors; see Appendix B and Section 7, respectively.

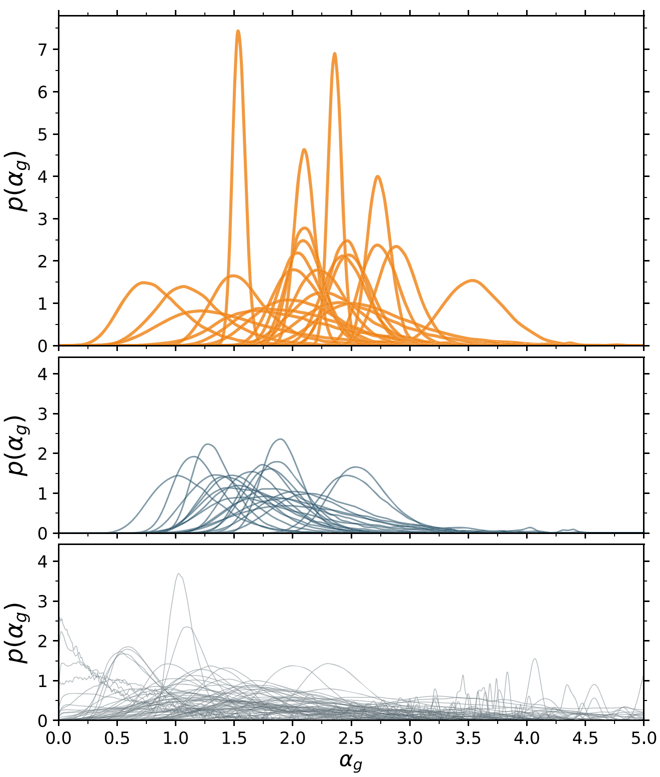

Figure 5. Marginalized posterior distribution of the rising power-law index in the g_{ZTF}-band, α_g, assuming a flat prior on α_g for individual SNe in our sample. Panels and color scheme are the same as in Figure 4. While the density of the PDFs tends toward 2, there is no support for a single mean power-law index to describe all SNe Ia.

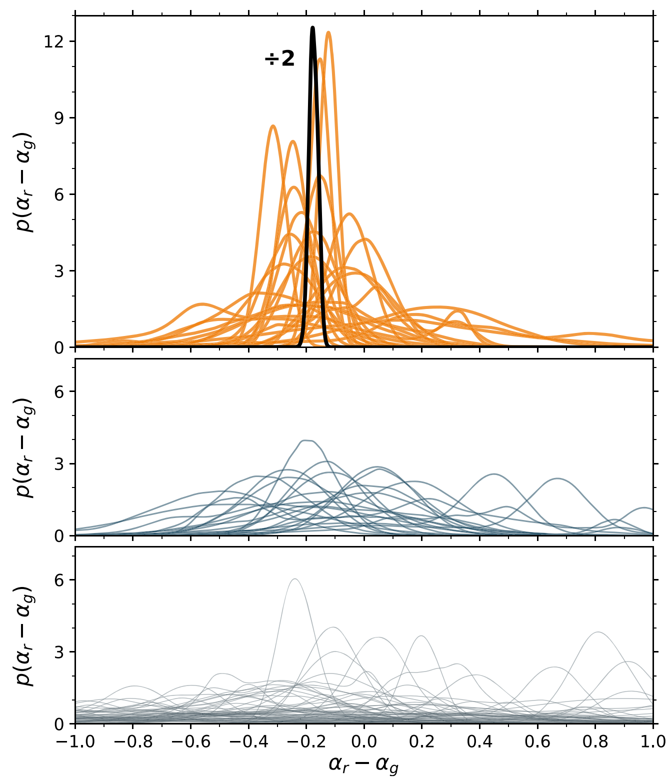

Figure 6. Marginalized posterior distribution of the early SN Ia color evolution, $\alpha_r - \alpha_g$, assuming flat priors on α_g and α_r. Panels and color scheme are the same as in Figure 4. Thick, solid black line shows an estimate of the mean value of $\alpha_r - \alpha_g$, which is estimated by multiplying together the likelihoods for SNe in the reliable-z_{host} group, which is why this mean is only shown in the top panel. For clarity, the mean PDF has been divided by 2. There is support for a single mean value of $\alpha_r - \alpha_g \approx -0.18$ (see Table 4).

correlation between t_{rise} and α_r. When including only models that do a good job of reproducing observations (see Section 5 in Magee et al. 2020), there is a strong correlation between t_{rise} and α_r (Spearman $\rho > 0.9$) that roughly matches the slope in Figure 7 (M. Magee 2020, private communication). It is therefore possible that the observed correlation between t_{rise} and α_r reflects the distribution of ^{56}Ni produced by thermonuclear explosions.

6.4. Correlations with Light-curve Shape

A defining characteristic of SNe Ia is that they can be described by a relatively simple luminosity–shape relation (Phillips 1993), which enables them to be used as standardizable candles. We examine the correlation between light-curve

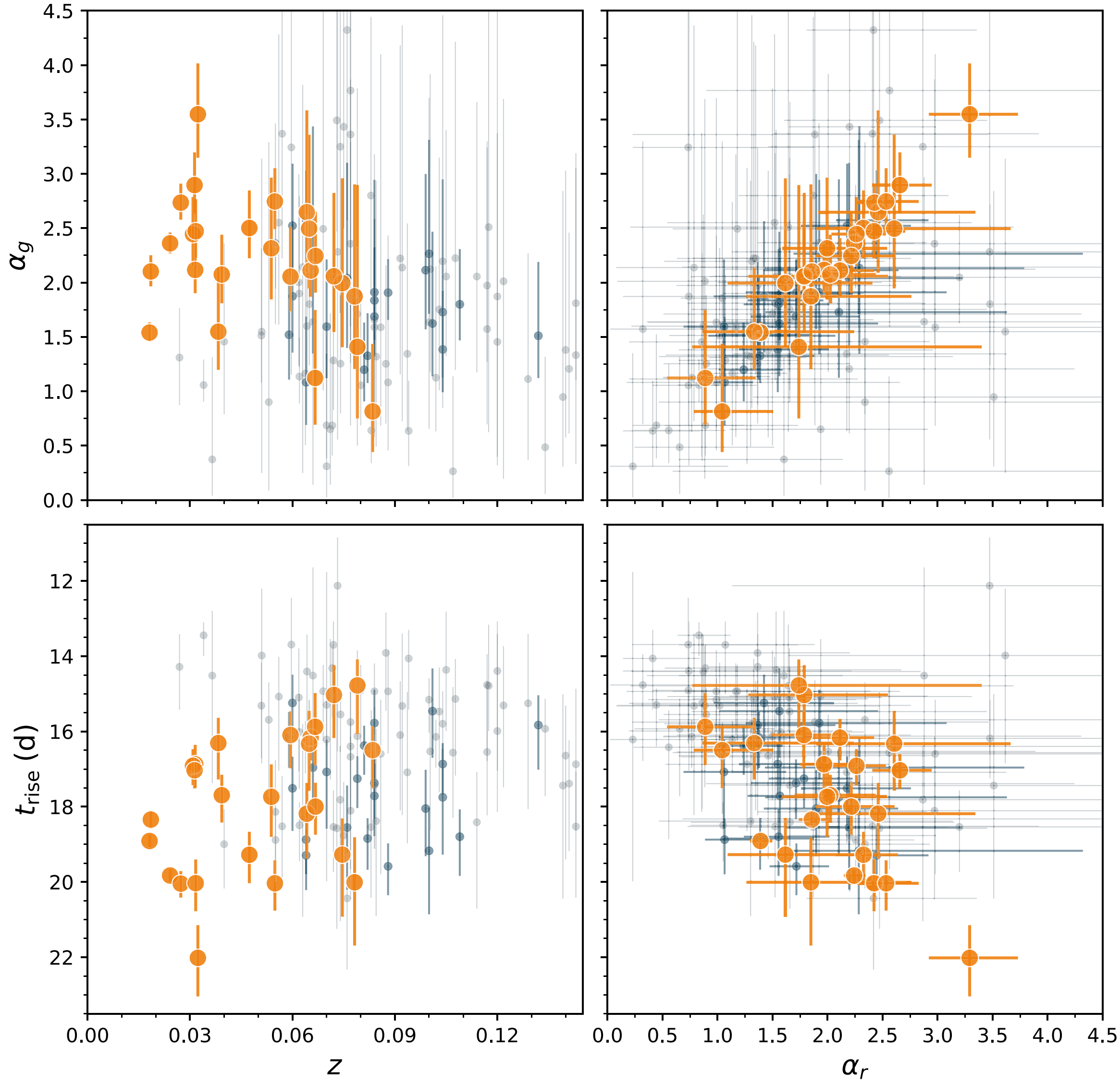

Figure 7. Correlation between redshift, z, SN rise time, $t_{\rm rise}$, and the power-law index in the $g_{\rm ZTF}$ and $r_{\rm ZTF}$ filters, α_g and α_r, respectively. We do not show α_r vs. z or $t_{\rm rise}$ vs. α_g, as these would largely be redundant given the very strong correlation between α_g and α_r (upper right panel). The sample has been divided into three groups: small, light gray circles show SNe from the unreliable group (see Appendix B); dark blue circles show the reliable-$z_{\rm SN}$ group; and large orange circles show the reliable-$z_{\rm host}$ group. The plots show that redshift is correlated with both $t_{\rm rise}$ and α_g, which would only be expected if SNe Ia undergo significant evolution from $z \approx 0$ to 0.1. We show this to be the result of a systematic selection effect (see text for further details).

shape, in this case the SALT2 x_1 parameter, and the SN rise time and α in Figure 9. There is a clear correlation between shape and $t_{\rm rise}$, which has been hinted at in other samples (e.g., Riess et al. 1999; González-Gaitán et al. 2012; Firth et al. 2015; Zheng et al. 2017). The Spearman coefficient for x_1 and $t_{\rm rise}$ is significant for the entire population ($\rho > 0.5$), and it increases when considering the reliable group ($\rho > 0.6$).

The x_1 shape parameter accounts for the width of both the SN rise and decline—and therefore, by definition, it should be correlated with the rise time. The middle and right panels of Figure 9 divide the reliable-$z_{\rm host}$ group into low ($z < 0.06$) and high ($z \geqslant 0.06$) redshift bins. From these panels, it is clear that some of the scatter in the x_1–$t_{\rm rise}$ plane is the result of the redshift bias discussed in Section 6.2, as higher-redshift SNe have shorter rise times at fixed x_1. A correction for this redshift effect would reduce the overall scatter seen in the lower panels of Figure 9 (see Section 7).

We compare separate measurements of the rise and decline of SNe Ia in Figure 10, which shows the correlation between $t_{\rm rise}$ and $\Delta m_{15}(g_{\rm ZTF})$, the observed decline in magnitudes of the $g_{\rm ZTF}$ light curve between the time of $g_{\rm ZTF}$ maximum light and 15 days later. The value of $\Delta m_{15}(g_{\rm ZTF})$ is measured via low-order polynomial fits to the rest-frame $g_{\rm ZTF}$ photometry (Kcorrections have been applied using the procedure in Bulla et al. (2020)), from an SN rest-frame phase $= -7$ to $+21$ days. This measurement is not possible for 16 of the 127 SNe in our sample, due to an insufficient number of observations in the defined window. Figure 10 shows that, on average, slowly declining SNe with smaller values of $\Delta m_{15}(g_{\rm ZTF})$ have longer rise times (Spearman $\rho \approx -0.4$ for the full sample, and ~ -0.5 for the reliable-$z_{\rm host}$ group).

While $t_{\rm rise}$ and $\Delta m_{15}(g_{\rm ZTF})$ exhibit a moderate correlation, a few SNe emerge as outliers relative to this relation. Among the low-z SNe in our sample, ZTF18abkhcrj (SN 2018emi) has

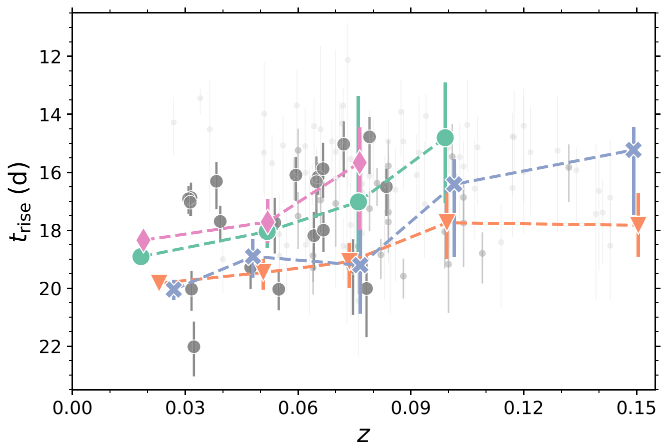

Figure 8. Same as the bottom left panel of Figure 7, though all SNe are shown in gray. Ther large green circle, magenta diamond, orange triangle, and purple *X* show how marginalized posterior estimates of $t_{\rm rise}$ change as the four lowest redshift SNe are observed at $z = 0.05$, 0.075, 0.1, and 0.15 (see text for further details). For clarity, slight offsets in z have been applied to the symbols, as the error bars would otherwise fully overlap. The value of $t_{\rm rise}$ clearly decreases with increasing redshift, showing that the observed correlation between these parameters is a consequence of flux-limited SN surveys.

$\Delta m_{15}(g_{\rm ZTF}) \approx 0.6$, making it a slow-declining SN, yet the rise time is a relatively short ∼16.3 days. In this particular case, the short rise time may be the result of larger photometric uncertainties than are typical for ZTF SNe. ZTF18abkhcrj (SN 2018emi) was discovered on top of the nucleus of its host galaxy during full moon. These two effects would contribute additional noise, delaying the phase at which the SN is discovered—and similar to the effects discussed in Section 6.2, yield a shorter estimate for $t_{\rm rise}$.

Hayden et al. (2010) find many SNe similar to ZTF18abkhcrj, in the sense that several of the slowest-declining SNe are among the fastest risers. Hayden et al. (2010) also find that the fastest-declining SN in their sample has $t_{\rm rise} > 20$ days. González-Gaitán et al. (2012) also find marginal evidence that slow-declining SNe have faster rise times than their fast-declining counterparts. The rise times in both Hayden et al. (2010) and González-Gaitán et al. (2012) are measured after shape correction, making it difficult to directly compare to our ZTF sample. Nevertheless, if there is no clear correlation, then that would suggest that the rise and fall of SNe Ia is set by different physics. Additional samples should be collected to test for this possibility.

There is no strong correlation between α and x_1 (Figure 9). The Spearman correlation for these two parameters is $\rho \approx -0.2$ whether looking at α_g or α_r, or whether considering the full sample, the reliable group, or the reliable-$z_{\rm host}$ group. Subdividing the reliable-$z_{\rm host}$ group by redshift shows the same trend that was identified in Figure 7: higher-redshift SNe have smaller values of α, on average, for the reliable-$z_{\rm host}$ group.

7. Strong Priors

7.1. Fixing $\alpha = 2$

In our previous effort to model the early evolution of SNe Ia, we adopted a flexible model (hereafter the "uninformative prior") allowing α and $t_{\rm fl}$ to simultaneously vary, despite theoretical (Arnett 1982; Riess et al. 1999) and observational (Conley et al. 2006; Hayden et al. 2010; Ganeshalingam et al. 2011; González-Gaitán et al. 2012) evidence that α is consistent with 2. Here, we alter the model by fixing $\alpha_g = \alpha_r = 2$ (hereafter the "$\alpha = 2$ prior"), and explore how this decision changes the results described in the previous sections. This decision is equivalent to placing an infinitely strong prior on the value of α.[22]

The distribution of rise-time PDFs using the $\alpha = 2$ prior is shown in Figure 11, and reported in Table 5. Adopting this strict prior significantly reduces the flexibility of the model. One consequence of this choice is that visual inspection of the posterior predictive flux values reveals that there are far fewer SNe with unreliable model parameters. When using the $\alpha = 2$ prior, we only flag SNe with an extrapolated flux using the maximum *a posteriori* model parameters $<0.9 f_{\rm max}$ at $T_{g,\rm max}$ as having unreliable model parameters. Based on this criterion, only five SNe are identified as having unreliable model parameters.

Figure 12 shows how the inferred rise time changes when adopting the $\alpha = 2$ prior instead of the uninformative prior for every SN in our sample. The $\alpha = 2$ prior reduces the uncertainty on $t_{\rm rise}$ (compare Figures 11 and 4) and increases the inferred rise time for each individual SN, with an average increase of ∼3 days in $t_{\rm rise}$.

Multiplying the individual likelihoods for $t_{\rm rise}$ does not provide support for a single mean rise time. Following the same approach described in Section 5.1, we find a population mean $t_{\rm rise} \approx 21.5$ days, with a corresponding population scatter of ∼2.0 days for the $\alpha = 2$ prior (see Table 4). Another consequence of adopting the $\alpha = 2$ prior is that a small handful (∼5–6) of SNe have rise times consistent with 26 days, which is considerably longer than the rise times inferred in any previous study of normal SNe Ia.

Figure 13 shows $t_{\rm rise}$ as a function of redshift (left) and x_1 (right) when adopting the $\alpha = 2$ prior. The previously observed trend where $t_{\rm rise}$ decreases at increasing redshifts is no longer seen. The model is, in effect, no longer flexible enough to systematically adjust $t_{\rm fl}$ to be approximately equal to the epoch of first detection. The removal of this particular bias provides a potential benefit of fixing $\alpha = 2$.

Adopting the $\alpha = 2$ prior yields a significantly smaller scatter in the correlation between x_1 and $t_{\rm rise}$, as shown in Figures 9 and 13. The reduction in this scatter intuitively makes sense, given that it was due, at least in part, to the redshift bias in measuring $t_{\rm rise}$ (Section 6.2). Reducing, or possibly fully removing, that bias by adopting the $\alpha = 2$ prior allows a direct estimate of the rise time from x_1 with a typical scatter <1 day. If relatively high-precision measurements of $t_{\rm rise}$ can be directly inferred from x_1, it would dramatically increase the sample of SNe Ia with measured rise times, as extremely early observations ($t < T_{B,\rm max} - 10$ days) would no longer be required (see Section 9.1.1).

7.2. Model Selection

In adopting two very different priors that, in turn, produce significantly different posteriors, we are naturally left with the question: which model is better? To some extent, the answer to this question rests with each individual, as the prior quantifies one's *a priori* belief about the model parameters. We posit that it is extremely unlikely that thermonuclear explosions

[22] Strictly enforcing $\alpha_g = \alpha_r$ imposes nonphysical structure on the models, as this condition effectively implies that there is no change in the $g - r$ color during the initial rise of the SN. This is clearly observed not to be the case in many SNe; see our Section 5.3, as well as Paper III in this series.

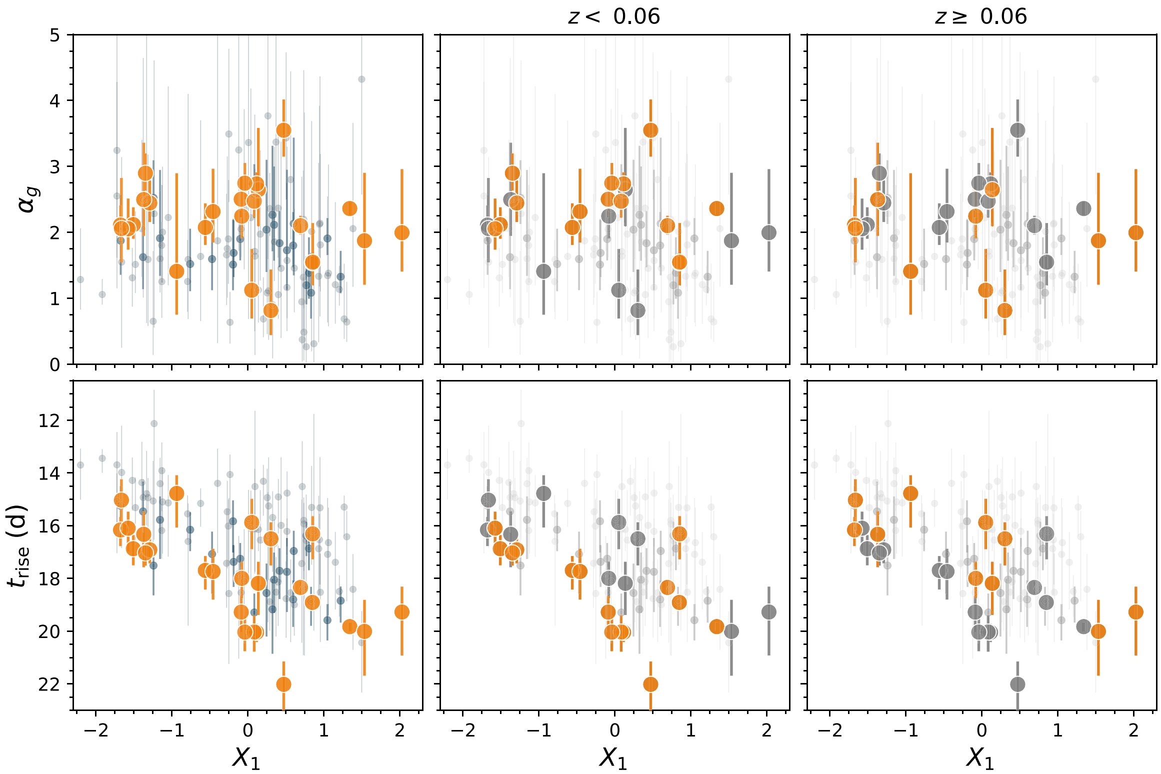

Figure 9. Correlation between the SALT2 x_1 shape parameter and α_g (top row) and $t_{\rm rise}$ (bottom row). Symbols are the same as in Figure 7. For clarity, the uncertainties on x_1 are not shown. Here, $t_{\rm rise}$ shows a strong correlation with x_1, while there is no correlation between α_g and x_1. The middle and right panels highlight reliable-$z_{\rm host}$ SNe at low, $z < 0.06$, and high, $z \geqslant 0.06$, redshift, respectively. Dividing the sample into different redshift bins shows that some of the observed scatter between x_1 and the model parameters is due to redshift and not intrinsic scatter.

all identically produce $\alpha = 2$ across a multitude of filters. Adopting $\alpha = 2$ is therefore very likely an overconfident position that produces slightly biased inferences.

Alternatively, we can address the question of which model is best via the use of model selection techniques based on information criteria. The uninformative prior includes more model parameters as α is allowed to vary. For individual SNe, we can compare the trade-off between increasing the model complexity, relative to the $\alpha = 2$ prior, and the overall improvement in the fit to the data in order to determine which model is superior. Following Spiegelhalter et al. (2002), we define the deviance D as

$$D(\theta) = -2\ln(p(x|\theta)) + C,$$

where θ represents the model parameters, x represents the observations, $p(x|\theta)$ is the likelihood, and C is a constant that will drop out following model comparison. From here, the effective number[23] of model parameters p_D can be calculated as:

$$p_D = \langle D(\theta)\rangle - D(\langle\theta\rangle),$$

where $\langle D(\theta)\rangle$ is the mean posterior value of the deviance, and $D(\langle\theta\rangle)$ is the deviance of the mean posterior model parameters. We then define the deviation information criterion (DIC) as:

$$\mathrm{DIC} = p_D + \langle D(\theta)\rangle.$$

Smaller values of the DIC are preferred to larger values.

Following Jeffreys (1961), we consider SNe with

$$\exp\left(\frac{\mathrm{DIC}_{\alpha 2} - \mathrm{DIC}_{\rm flat}}{2}\right) \geqslant 30,$$

where $\mathrm{DIC}_{\alpha 2}$ is the DIC for the $\alpha = 2$ prior and $\mathrm{DIC}_{\rm flat}$ is the DIC for the uninformative prior, to exhibit a very strong preference for the uninformative prior. Of the 127 SNe in our sample, including the 7 SNe that are not considered normal SNe Ia, only 29 show a strong preference for the uninformative prior. Of these 29 SNe, 16 belong to the unreliable group. Visual inspection of these 16 confirms that these SNe have very few detections after $t_{\rm fl}$. In these cases, the data are fit extremely well with very small values of α (see, e.g., Figure B1). The remaining 13 SNe are at low z, with few, if any, gaps in observational coverage.

Thus, the $\alpha = 2$ prior should be used to estimate $t_{\rm fl}$ for all but 13 SNe in our sample. For these 13, the uninformative prior provides a better estimate of $t_{\rm fl}$, according to the DIC. This combination of results is how we define the distribution of $t_{\rm fl}$ in Paper III of this series (Bulla et al. 2020).

[23] Many model selection techniques based on information criteria, such as the Akaike information criterion (AIC; Akaike 1974) or "Bayesian" information criterion (BIC; Schwarz 1978), include a point estimate of the maximized likelihood and then subtract a penalty term related to the total number of parameters in the model. These methods aim to balance the goodness of fit while regulating the overall model complexity. The AIC and BIC cannot, however, easily be applied to the models adopted here, as the use of an informative prior distribution reduces the amount of overfitting and produces an "effective" number of parameters that is smaller than the number of variables in the parameterized model (Gelman et al. 2014). We adopt the DIC, as opposed to the AIC or BIC, because it effectively marginalizes over the nuisance parameters and applies to the full set of posterior predictions.

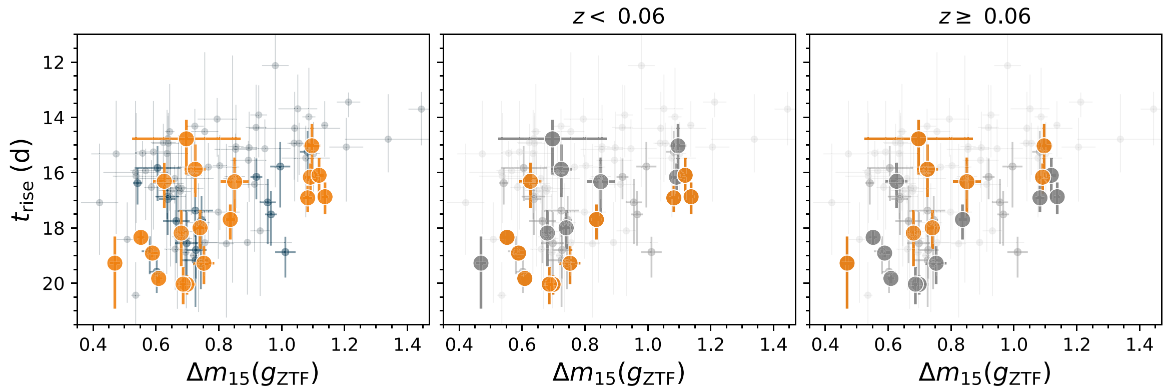

Figure 10. Correlation between $\Delta m_{15}(g_{ZTF})$ and t_{rise}. Symbols are the same as in Figure 7. There is a clear correlation between the rise and decline times of SNe Ia. Some of the scatter in the relationship between these parameters can be explained as a result of the redshift effect discussed in Section 6.2.

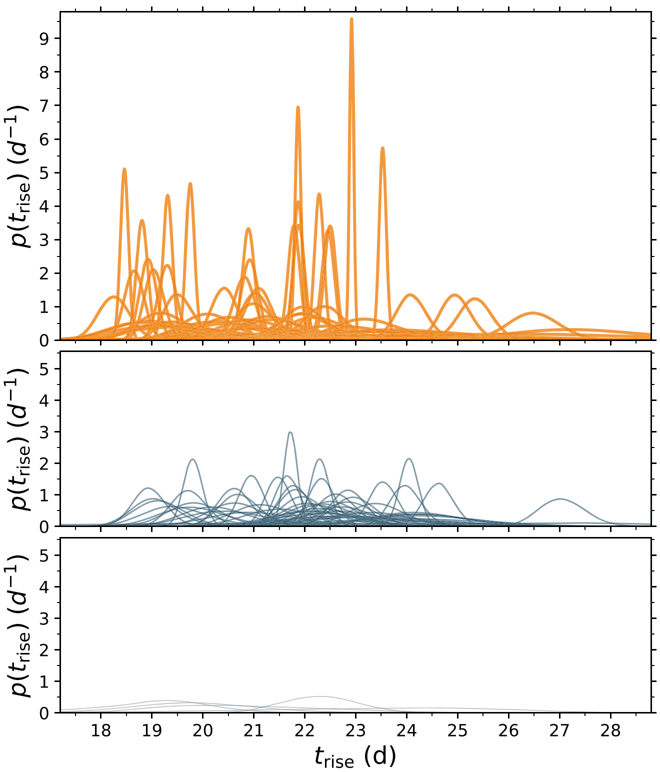

Figure 11. Same as Figure 4, showing the resulting PDFs for the $\alpha = 2$ prior. Note that the definition for reliable model parameters with the $\alpha = 2$ prior is different from that described in Appendix B (see text). As was the case when α is allowed to vary, there is no support for a single mean t_{rise} to describe every SN in the sample. The $\alpha = 2$ prior results in rise times that are ∼3 days longer on average.

Table 5
Ninety Percent Credible Region for t_{rise} ($\alpha = 2$ Prior)

		t_{rise}(day)			
ZTF Name	TNS Name	5	50	95	Reliable[a]
ZTF18aailmnv	SN 2018ebo	21.01	22.22	23.65	y
ZTF18aansqun	SN 2018dyp	17.82	19.22	20.88	y
ZTF18aaoxryq	SN 2018ert	21.02	23.21	26.34	y
ZTF18aapqwyv	SN 2018bhc	17.83	18.95	20.53	y
ZTF18aapsedq	SN 2018bgs	21.71	22.38	23.03	y
ZTF18aaqcozd	SN 2018bjc	18.12	19.59	21.52	y
ZTF18aaqcqkv	SN 2018lpc	17.62	19.79	22.13	n
ZTF18aaqcqvr	SN 2018bvg	21.18	21.98	22.91	y
ZTF18aaqcugm	SN 2018bhi	19.06	19.52	20.04	y
ZTF18aaqffyp	SN 2018bhr	17.91	23.36	26.79	n
ZTF18aaqnrum	SN 2018bhs	16.47	22.55	25.51	y
ZTF18aaqqoqs	SN 2018cbh	24.15	24.62	25.12	y
ZTF18aarldnh	SN 2018lpd	19.32	20.57	22.04	y
ZTF18aarqnje	SN 2018bvd	20.40	21.55	22.83	y
ZTF18aasdted	SN 2018big	23.42	23.53	23.65	y

Notes.
The table includes the 5th, 50th, and 95th percentiles for t_{rise} after adopting the $\alpha = 2$ prior (see text for further details).
[a] Flag for SNe with reliable model parameters. Note that the $\alpha = 2$ prior definition of reliable differs from that in Appendix B (see text).
(This table is available in its entirety in machine-readable form.)

8. A Volume-limited Sample of Normal SNe Ia

The ZTF sample of SNe Ia is clearly biased due to Malmquist selection effects (see Yao et al. 2019), and as such, the population results discussed above are also correspondingly biased. We can, however, approximate a volume-limited subset of *normal* SNe Ia. A full study of the completeness of the ZTF SN Ia sample is beyond the scope of this paper and will be discussed in a future study (J. Nordin et al. 2020, in preparation).

The selection criteria presented in Paper I removes SNe Ia from the sample if they lack a g_{ZTF} detection >10 days prior to $T_{B,max}$ (Yao et al. 2019). By construction, the intrinsically faintest normal SNe Ia in the ZTF sample have $x_1 \approx -2$, with $M_g \approx -17$ mag at $t \approx -10$ days. With a typical limiting magnitude of $g_{ztf} \approx 20.0$ mag during bright time (Bellm et al. 2019b), the ZTF high-cadence survey should be complete to all $x_1 \approx -2$ and brighter SNe to a distance modulus $\mu \approx 37$ mag. For our adopted cosmology, this distance corresponds to a redshift $z \approx 0.0585$. Thus, the 28 normal SNe Ia with $z < 0.06$ should comprise a volume-limited subset of our sample.

For the uninformative prior, 16 of the 28 low-redshift SNe have reliable model parameters, and 15 of those 16 have known host redshifts. Using the same procedure as Section 5.1, we estimate a weighted mean rise time of ∼18.9 days when considering the volume complete subset ($z < 0.06$) of our sample (see Table 4 for the mean values discussed here and in the remainder of this section). For these SNe, we also find mean values of ∼2.13 and ∼2.01 for α_g and α_r, respectively.

For the $\alpha = 2$ prior, 27 of the 28 low-redshift SNe have reliable model parameters, and 24 of those 27 have known host redshifts. For this prior, we estimate a weighted mean rise time of ∼21.7 days.

If we instead use the results from the $\alpha = 2$ prior, unless the DIC provides very strong evidence for the uninformative prior, as suggested at the end of Section 7.2, then we find a mean rise time of ∼19.9 days for the volume-limited sample. It makes sense that this mean is nearly 2 days shorter than the mean for the $\alpha = 2$ prior, because the SNe for which the DIC prefers the uninformative prior provide the lowest variance estimates of $t_{\rm rise}$.

Finally, if examine only those SNe for which the DIC prefers the uninformative prior, of which there are only nine normal SNe with $z < 0.06$ (all of which have known $z_{\rm host}$) in our entire sample, we find a mean rise time of 19.20 ± 0.06. For this same subset, we find mean values of α_g and α_r of 2.14 ± 0.03 and 2.02 ± 0.03, respectively.

Given the bias identified in Section 6.2, it is not surprising that a volume-limited sample of SNe has larger estimates for the mean values of $t_{\rm rise}$ and α, when using the uninformative prior. For the $\alpha = 2$ prior, on the other hand, the volume-limited sample produces very similar estimates for the mean $t_{\rm rise}$ (<1% difference) and the full sample. This provides additional evidence that the adoption of a strong prior can negate the redshift bias highlighted in Section 6.2.

9. Discussion

9.1. SNe Ia Rise Times

In the analysis above, we provide multiple measurements of the rise time of SNe Ia following the adoption of different priors. Within the literature, there are at least a half dozen entirely different methods that have been employed to answer precisely the same question. This naturally raises the question—which method is best? Answering that question in turn raises an important offshoot as well—is the method cheap to implement (i.e., does it provide reliable inference in the limit of poor sampling or low S/N)?

9.1.1. SALT2 x_1 as a Proxy for t_{rise}

Estimating the rise times of SNe Ia using only observations around maximum brightness would be an ideal approach. This approach would maximize the sample size from flux-limited surveys, and Figure 13 suggests it may be feasible given the correlation between the SALT2 x_1 parameter and $t_{\rm rise}$ (measured using the $\alpha = 2$ prior).[24] Even in the limit of only one or a few observations on the rise, SALT2 can still measure x_1 (e.g., Scolnic et al. 2018). Therefore, the correlation between x_1 and $t_{\rm rise}$ eliminates the need for high-cadence observations to yield early (>10 days prior to $T_{B,\rm max}$) discoveries, enabling a more economical method to estimate $t_{\rm rise}$ relative to the methods described above.

For the volume-limited sample (see Section 8) of normal SNe Ia with known host galaxy redshifts and reliable model parameters, we estimate the relation between $t_{\rm rise}$ and x_1 via a maximum-likelihood linear fit that accounts for the uncertainties on both $t_{\rm rise}$ and x_1 (see Hogg et al. 2010). From this fit, we find

$$t_{\rm rise} = (21.41 \pm 0.03) + (1.62 \pm 0.03)x_1 \text{ day}. \quad (3)$$

[24] Other shape parameters, such as the stretch, s, or distance from a fiducial template, Δ, may work in place of x_1.

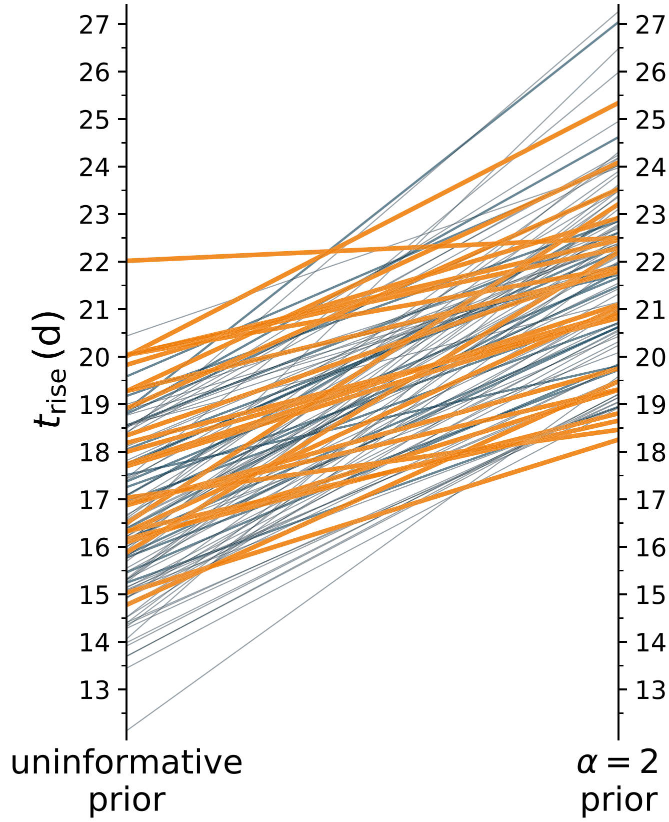

Figure 12. Comparison of the rise time inferred when adopting the uninformative prior and the $\alpha = 2$ prior for the 120 normal SNe in our sample. Adoption of the $\alpha = 2$ prior leads to larger values of $t_{\rm rise}$ for every SN, with an average increase of ∼3 days. Individual lines are colored orange, dark blue, and gray for the uninformative prior reliable-$z_{\rm host}$, reliable-$z_{\rm SN}$, and unreliable groups, respectively.

The residual scatter about this relation, as estimated by the sample standard deviation, is 0.81 day. We find the relation does not significantly change when including SNe with unknown host-galaxy redshifts or unreliable model parameters (though the scatter increases to ∼1.2 days when including $z \geqslant 0.06$ SNe in the fit). Thus, if one assumes $\alpha = 2$, then SALT2 can be used to estimate $t_{\rm rise}$ with a typical uncertainty of ∼0.8 day. This scatter is only slightly worse than the median uncertainty on $t_{\rm rise}$, ∼0.5 day, for individual SNe when adopting the $\alpha = 2$ prior (see Section 7). Furthermore, given that an $x_1 = 0$ SN is supposed to represent a "mean" SN Ia, Equation (3) suggests that the mean rise time of SNe Ia is ∼21.4 days.

If we repeat the same exercise using uninformative prior rise times for the volume limited sample, we find that the typical scatter about the linear $t_{\rm rise}$–x_1 relation is ∼1.7 days and ∼1.4 days for the full sample and reliable group, respectively. The rise time of a mean SN according to this relation is ∼18.4 days; however, we caution that some individual rise time measurements for this prior may be underestimated as discussed in Section 6.2.

9.1.2. Precise Estimates of t_{rise} from Early Observations

While the $t_{\rm rise}$–x_1 relation provides a relatively cheap method to infer the rise time of normal SNe Ia, a significant advantage of early observations is that they can provide far more precise

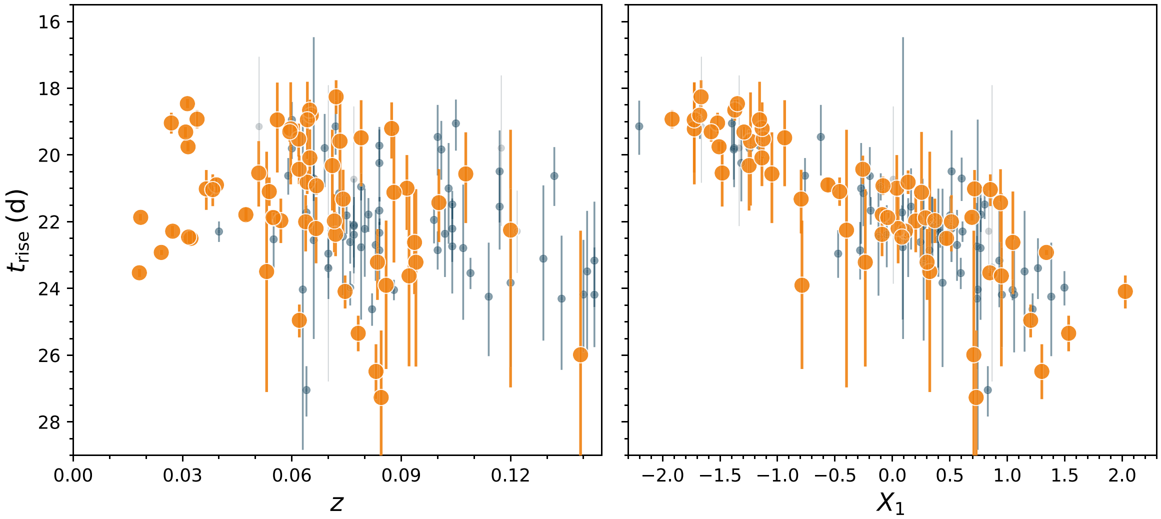

Figure 13. Correlation between $t_{\rm rise}$ and redshift (left) and x_1 (right) when adopting the $\alpha = 2$ prior for the early emission from SNe Ia. Use of this strict prior removes the previously observed bias that resulted in shorter rise times being inferred at higher redshifts. One consequence of the removal of this bias is a reduction in the observed scatter between $t_{\rm rise}$ and x_1.

estimates of $t_{\rm rise}$, especially in the limit of high S/N. For the $\alpha = 2$ prior, there are 14 SNe with a half 68% credible region that is <3 hr. For the uninformative prior, this number drops to two SNe. In either case, these measurements provide far more precision than possible from extrapolations based on SN Ia shape parameters (such as x_1).

While the methods adopted in this paper provide higher precision, it is impossible that they are both accurate. The median difference in the inferred $t_{\rm rise}$ from the $\alpha = 2$ and uninformative priors for individual SNe is 4.9 days. Even the volume-limited subset of SNe with reliable model parameters from the uninformative prior (15 total SNe) have a median difference of 2.9 days in $t_{\rm rise}$ for the two priors. The systematic effect identified in Section 6.2 suggests that the uninformative prior does not provide accurate estimates of $t_{\rm rise}$ for higher-z SNe. The $\alpha = 2$ prior, on the other hand, explicitly assumes that there is no change in the early optical color of SNe Ia. Many SNe with early observations clearly invalidate this particular assumption, raising the possibility that neither method is accurate.

An SN cannot be detected until it has exploded, and thus the epoch of discovery provides a lower limit on $t_{\rm rise}$. Between PTF/iPTF (Papadogiannakis et al. 2019) and ZTF (Yao et al. 2019), there are ∼20 SNe Ia that are detected at least 18 days before $T_{B,\rm max}$, with a few detections as early as 21 days before $T_{B,\rm max}$. If the uninformative prior is accurate, then each of these SNe would represent an incredibly lucky set of circumstances: (i) they each have longer rise times than average (∼18 days; see Section 8), and (ii) they were all discovered more or less immediately after $t_{\rm fl}$. A more probable explanation is that the mean rise time is >18 days, in which case the $\alpha = 2$ prior may provide a more accurate inference of the rise time (though again we caution that these estimates may also be inaccurate). The fact that each of the four SNe with $z < 0.03$, which should have the least biased rise time estimates (see Section 6.2), have $t_{\rm rise} > 18$ days, further supports this claim.

9.1.3. Comparison to the Literature

Several studies in the literature have attempted to measure the mean rise time of SNe Ia. Here, we compare our work to previous results. This exercise is somewhat fraught with difficulty, in the sense that each study incorporates slight differences in implementation, which in turn makes comparisons challenging. Furthermore, these studies are typically conducted with different filter sets and over a wide range of redshifts, which may introduce biases that are difficult to quantify across studies (as discussed above, *K*corrections are highly uncertain at very early epochs). Finally, the quality of the data in each of these studies is vastly different. For example, in Riess et al. (1999) there are only six SNe (and 10 total *B*-band observations) observed at phases $\leqslant -15$ days, while our study includes 31 SNe *discovered >15 days before* $T_{B,\rm max}$ (Yao et al. 2019). As we proceed with our cross-study comparison, we exclude rise time estimates for individual SNe and instead focus on studies with relatively large samples ($\gtrsim 10$ normal SNe Ia).

As outlined in the introduction, there are broadly two different methods to measure the mean rise time of SNe Ia. The first uses the well-established luminosity–decline relation for SNe Ia (Phillips 1993) to "shape correct" the SN light curves prior to fitting for the rise time. Thus, individual light curves are stretched by some empirically measured factor, and the mean rise time represents a normal SN Ia *after shape correction* (e.g., Riess et al. 1999; Aldering et al. 2000; Conley et al. 2006; Hayden et al. 2010; Ganeshalingam et al. 2011; González-Gaitán et al. 2012). The second method measures the rise time of each SN Ia within a sample, and then takes the mean of this distribution. These two methods are not equivalent, and therefore are likely to produce different results. If, for instance, a flux-limited survey finds more high-luminosity, slower-declining SNe than low-luminosity, faster-declining events, then the population mean will produce longer rise times than the shape-corrected mean.

Using different data sets obtained in very different redshift regimes, Riess et al. (1999), Aldering et al. (2000), and Conley et al. (2006) estimate consistent values of the shape-corrected mean $t_{\rm rise} \approx 19.5$ days. Each of these studies fixes $\alpha = 2$ when fitting for the rise time. This estimate is similar to, though slightly longer, than our estimate for the mean rise time in the reliable, volume-limited subset of our sample (see Section 8). Later studies by Hayden et al. (2010), Ganeshalingam et al. (2011), and González-Gaitán et al. (2012) also provide estimates of the mean shape-corrected rise time and find smaller values of ~17.0–18.0 days. As noted by Hayden et al., these methods are highly dependent on the template light curve used to stretch the individual SNe, and differences in the templates used by each study may explain the dissensus between their findings.

The approach employed in Firth et al. (2015), Zheng et al. (2017), and Papadogiannakis et al. (2019) is more similar to the one adopted here. Each of these studies estimates $t_{\rm rise}$ for individual SNe and then calculates the population mean. If the samples differ between any of these studies—and aside from 11 SNe that are included in both Papadogiannakis et al. (2019) and Firth et al. (2015), there is no overlap between any of those studies or this one—then it should be expected that the population mean rise time estimates will differ. Furthermore, the $t_{\rm rise}$ estimates in Papadogiannakis et al. (2019) and Firth et al. (2015) are not relative to $T_{B,\rm max}$, and it is known that the rise time varies as a function of wavelength (e.g., Ganeshalingam et al. 2011). Taken together, this confluence of factors makes it difficult to compare results between these studies, which we nevertheless do below.

In Zheng & Filippenko (2017), a semi-analytical, six-parameter, broken power-law model is introduced to describe the optical evolution of SNe Ia. This model has a distinct advantage over the methods employed here, in that an artificial cutoff does not need to be applied in flux space (see Section 4), though a post-peak cut must be applied as the model cannot reproduce the evolution of SNe into the nebular phase. A downside of this approach is that there are large degeneracies between the different model parameters, meaning it is difficult to find numerically stable solutions without fixing individual parameters to a single value (Zheng et al. 2017). For a sample of 56 well-observed low-z SNe, this method produces a mean rise time of 16.0 days (Zheng et al. 2017), while the same technique applied to SNe Ia from PTF/iPTF finds a mean rise time of 16.8 days (Papadogiannakis et al. 2019). These estimates are considerably lower than the ones presented here, and are almost certainly underestimates of the true mean rise time based on the large number of SNe with detections >16 days before peak (Papadogiannakis et al. 2019; Yao et al. 2019). Indeed, inspection of Figure 1 in Zheng et al. (2017) shows that the six-parameter model underestimates the flux at the very earliest epochs and underestimates $t_{\rm rise}$ as a result.

The closest comparison to the methods used in this study can be drawn from Firth et al. (2015). Using a sample of 18 SNe discovered by PTF and the La Silla Quest (LSQ) survey, Firth et al. fit a model similar to Equation (1), in that $t_{\rm fl}$ and α are allowed to simultaneously vary. From these fits, they estimate a mean population $t_{\rm rise} = 18.98 \pm 0.54$ days, which is consistent with our estimate of the rise time for the volume-complete $z_{\rm host}$ sample, ~18.9 days. Contrary to this study, they find shorter rise times and a mean of ~17.9 days, when fixing $\alpha = 2$ (this is likely explained by their adopted fit procedure; see Section 9.2).

9.2. The Expanding Fireball Model

The expanding fireball model (see Section 4) is remarkable in its simplicity. Its two underlying assumptions, that the photospheric velocity and temperature of the ejecta are approximately constant during the early evolution of the SN, are clearly oversimplifications; Parrent et al. (2012) show that the photospheric velocity declines by at least 33% in the ~5 days after explosion. Despite these simplifications, numerous studies have found that α is consistent with 2 (e.g., Conley et al. 2006; Hayden et al. 2010; Ganeshalingam et al. 2011; González-Gaitán et al. 2012; Zheng et al. 2017).

Based on the volume-limited subset of normal SNe Ia with reliable model parameters, we find a population mean $\alpha_r = 2.01 \pm 0.03$, which is consistent with the expanding fireball model. For α_g, on the other hand, we find a population mean of 2.13 ± 0.03, which is only marginally consistent with 2. As previously noted, a power-law index of 2 in every optical filter would stand in contrast to observations, as it would imply that SNe Ia have no color evolution shortly after explosion.

Furthermore, there are individual normal SNe Ia for which the expanding fireball model does not apply. There are several examples within the literature (e.g., Zheng et al. 2013, 2014; Goobar et al. 2015; Miller et al. 2018; Dimitriadis et al. 2019; Shappee et al. 2019), and within this study, several low-z SNe are inconsistent with the expanding fireball model:

1. ZTF18aasdted (SN 2018big; $z \approx 0.018$, $\alpha_r \approx 1.4$),
2. ZTF18abauprj (SN 2018cnw; $z \approx 0.024$, $\alpha_r \approx 2.2$),
3. ZTF18abcflnz (SN 2018cuw; $z \approx 0.027$, $\alpha_r \approx 2.4$),
4. ZTF18abfhryc (SN 2018dhw; $z \approx 0.032$, $\alpha_r \approx 3.3$),
5. ZTF18abuqugw (SN 2018geo; $z \approx 0.031$, $\alpha_r \approx 2.7$).

In each of these cases, the DIC clearly prefers $\alpha \neq 2$.

Given that many of the very best-observed, low-redshift SNe are incompatible with $\alpha = 2$, and that the mean $\alpha_g > 2$ in the ZTF sample, it is clear that the expanding fireball model does not adequately reproduce the observed diversity of SNe Ia. Nevertheless, according to the DIC, $\alpha = 2$ provides a reasonable proxy for the early evolution of the majority of normal SNe Ia (at the quality of ZTF high-cadence observations). This is either telling us that individual SNe exhibiting significant departures from $\alpha = 2$ are atypical—an interpretation adopted in Hosseinzadeh et al. (2017), Miller et al. (2018), Dimitriadis et al. (2019) and elsewhere—or that, for the vast majority of SNe, the observations are not of high enough quality to conclusively show $\alpha \neq 2$. Distinguishing between these two possibilities requires larger volume-limited samples.

Moving forward, it may be that the most appropriate prior for fitting the early evolution of SNe Ia is to adopt a Gaussian centered at 2 for α in the redder filters, while also placing a prior on the difference in α across different filters (for ZTF $\alpha_r - \alpha_g \approx -0.18$, based on Section 5.3). More testing and observations, especially of low-z SNe, are needed to confirm whether or not such priors are in fact appropriate.

Finally, we note that the analysis in Firth et al. (2015) finds a mean value of $\alpha = 2.44 \pm 0.13$, which is not consistent with 2. This result can be understood in the context of the Firth et al. (2015) fitting procedure, whereby an initial estimate of $t_{\rm fl}$ is made by fixing $\alpha = 2$. Only observations obtained 2 days before and after this initial $t_{\rm fl}$ estimate are included in the final model fit (i.e., the entire baseline of nondetections is not used, as is done in this study). Truncating the baseline biases the model to longer rise times (as is observed in Firth et al. (2015)), and as shown in Figures 1–3, longer rise times require larger values of α when adopting a simple power-law model (as is done here and in Firth et al. (2015)).

The reason it is critical to test the expanding fireball model is that robust measurements of α can distinguish between different explosion scenarios. For example, the delayed-detonation models presented in Blondin et al. (2013), which provide a good match to SNe Ia at maximum light, systematically overestimate the power-law index at early times (with typical values of $\alpha \approx 7$; see Figure 1 in Dessart et al. (2014)). This led Dessart et al. (2014) to alternatively consider pulsational-delayed detonation models, which do result in a smaller power-law index ($\alpha \approx 3$), though those results are still incompatible with what we find here.[25] In Noebauer et al. (2017), the early evolution of various explosion models does not follow an exact power law. They find an almost power-law evolution for pure deflagration models, which may explain the origin of SN 2002cx-like SNe. For pure deflagrations, Noebauer et al. (2017) find $\alpha < 2$, which qualitatively agrees with our results for ZTF18abclfee (SN 2018cxk), where $\alpha_r \approx 1$ (see Appendix C). The models presented in Magee et al. (2020), which examine the evolution of SNe with different ^{56}Ni distributions, provide good qualitative agreement to what we find for ZTF SNe. Magee et al. (2020) find that the rising power-law index is larger in the Bband than the Rband (similar to what we see in $g_{\rm ZTF}$ and $r_{\rm ZTF}$), and that the mean value of these distributions is ∼2. As suggested in Magee et al. (2020), it may be the case that the vast majority of the differences observed in the early ZTF light curves can be explained via variations in the ^{56}Ni mixing in the SN ejecta. Future modeling will test this possibility (M. Deckers et al. 2020, in preparation).

10. Conclusions

In this paper, we have presented an analysis of the initial evolution and rise times of 127 ZTF-discovered SNe Ia with early observations; see Yao et al. (2019) for details on how the sample was selected. These SNe were observed as part of the ZTF high-cadence extragalactic experiment, which obtained three $g_{\rm ZTF}$ and three $r_{\rm ZTF}$ observations every night the telescope was open. A key distinction of this data set, in contrast to many previous studies, is the large number of observations taken prior to the epoch of discovery, which meaningfully constrains the behavior of the SN at very early times (see Appendix D.2). The uniformity, size, and observational duty cycle of this data set are truly unique, making this sample of ZTF SNe the premier data set for studying the early evolution of thermonuclear SNe.

We model the emission from these SNe as a power law in time t, whereby the flux $f \propto (t - t_{\rm fl})^{\alpha}$, where $t_{\rm fl}$ is the time of first light, and α is the power-law index. By simultaneously fitting observations in the $g_{\rm ZTF}$ and $r_{\rm ZTF}$ filters, we are able to place stronger constraints on $t_{\rm fl}$ than would be possible with observations in a single filter. While many previous studies have fixed $\alpha = 2$, following the simple expanding fireball model (e.g., Riess et al. 1999), we have instead allowed α to vary, as there are recent examples of SNe Ia where α clearly is not equal to 2 (e.g., Zheng et al. 2013, 2014; Goobar et al. 2015; Miller et al. 2018; Dimitriadis et al. 2019; Shappee et al. 2019). While the population mean value of α tends toward 2, there are several individual SNe featuring an early evolution that deviates from an $\alpha = 2$ power law, justifying our model parameterization.

[25] The range of α values reported in Dessart et al. (2014) is fit to the first ∼3 days after explosion. Fitting all observations with $f_{\rm obs} \leqslant 0.4 f_{\rm max}$, as is done in this study, would reduce the inferred values of α in Dessart et al. (2014).

As might be expected, we find that our ability to constrain the model parameters is highly dependent on the quality of the data. SNe Ia at low redshifts that lack significant gaps in observational coverage are better constrained than their high-redshift counterparts or events with large temporal gaps. We identify those SNe with reliable model parameters under the reasonable assumption that models of the initial flux evolution should overestimate the flux at peak brightness. Following this procedure, we find that 51 of the SNe have reliable model parameters. We focus our analysis on these events.

For the subset of normal SNe with reliable model parameters, we estimate a population mean $t_{\rm rise} \approx 18.5$ days, with a sample standard deviation of ∼1.6 days. For individual SNe, the range of rise times extends from ∼15 to 22 days. We have additionally identified a systematic in the parameter estimation for models that simultaneously vary $t_{\rm fl}$ and α. Namely, for flux-limited surveys, the model constraints on $t_{\rm rise}$ will be systematically underestimated for the higher redshift SNe in the sample. If we restrict the sample to a volume-limited subset of SNe ($z < 0.06$), where this bias may still be present but probably less prevalent, we estimate a mean population rise time of ∼18.9 days.

Normal SNe Ia have a population mean $\alpha_g \approx 2.1$ and a population mean $\alpha_r \approx 2.0$, with a population standard deviation ∼0.5 for both parameters. While the mean value for our sample of SNe tends toward 2, we observe a range in α extending from ∼1.0 to 3.5. For both $t_{\rm rise}$ and α, there is no single value that is consistent with all the SNe in our sample. Interestingly, we find that nearly all SNe are consistent with a single value of $\alpha_r - \alpha_g$, which describes the initial $g_{\rm ZTF}$−$r_{\rm ZTF}$ color evolution of SNe Ia. The data show a mean value of $\alpha_r - \alpha_g \approx -0.18$, meaning the optical colors of most SNe Ia evolve to the blue with comparable magnitudes over a similar timescale. This could be a sign that the degree of ^{56}Ni-mixing in the SN ejecta is very similar for the majority of SNe Ia (e.g., Piro & Morozova 2016; Magee et al. 2018, 2020).

We find that the rise time is correlated with the light-curve shape of the SN, in the sense that high-luminosity, slowly declining SNe have longer rise times. This finding is consistent with many previous studies.

Given the large number of SNe with unreliable model parameters, in addition to the observed bias in the measurement of $t_{\rm rise}$ for high-z SNe, we also consider how the model parameter estimates change with strong priors. In particular, we adopt $\alpha_g = \alpha_r = 2$, enforcing the expanding fireball hypothesis on the data. Strictly speaking, this prior means that the early colors of SNe Ia do not change, which we empirically know is not the case. Nevertheless, a nearly constant temperature is one of the assumptions of the fireball model, and thus we proceed.

Under the $\alpha = 2$ prior, we find that far more SNe have reliable $t_{\rm rise}$ estimates. For the typical SN in our sample, fixing $\alpha = 2$ results in an increase in $t_{\rm rise}$ by a few days. We estimate a population mean $t_{\rm rise} \approx 21.6$ days when adopting the $\alpha = 2$ prior. One consequence of adopting this prior is that it significantly reduces the previously observed bias where high-z SNe are inferred to have shorter rise times. The use of this prior also reduces the scatter in the x_1–$t_{\rm rise}$ relation, and we find that with SALT2, via the measurement of x_1, it is possible to estimate $t_{\rm rise}$ with a typical scatter of ∼0.81 day, even if there are no early-time observations available. We also find that, for the vast majority of the SNe in our sample (all but 13 events), there is at best only weak evidence that the $\alpha \neq 2$ model is preferred to a model with $\alpha_g = \alpha_r = 2$ according to the DIC.

While we have primarily focused on the properties and evolution of normal SNe Ia, there are seven SNe in our sample that cannot be categorized as normal (see Yao et al. 2019). In Appendix C, we find that the rise times of Ia-CSM SNe and SC explosions are longer than those of normal SNe Ia, in accordance with previous studies. We highlight our observations of ZTF18abclfee (SN 2018cxk), an SN 2002cx-like SN with exquisite observational coverage in the time before explosion. We estimate $t_{\rm fl}$ to within ∼8 hr for ZTF18abclfee, making our measurement the most precise estimate of $t_{\rm rise}$ for any 02cx-like SN to date. ZTF18abclfee took ∼10 days to reach peak brightness, roughly five days less than SN 2005hk, another 02cx-like event with a well-constrained rise time.

This study has important implications for future efforts to characterize the rise times of SNe Ia. We have found that, for all but the best-observed, highest S/N events, a generic power-law model where α is allowed to vary does not place meaningful constraints on the rise time—or worse, in the case of higher-z events, it produces a biased estimate. If this were the end of the story, it would be particularly bad news for LSST, which will typically have gaps of several days in its observational cadence (Ivezić et al. 2019). With only Equation (1) at our disposal, we would rarely be able to infer $t_{\rm rise}$ for LSST SNe. As we demonstrated with the $\alpha = 2$ prior, in the limit of low-quality data, the application of a strong prior can significantly improve the final inference. Our current challenge is to develop an empirically motivated prior for the model parameters. This provides a strong justification for the concurrent operation of LSST and small-aperture, high-cadence experiments, such as ZTF and the planned ZTF-II. These smaller, more focused, missions can provide exquisite observations of a select handful of SNe that can be used to drive the priors in our inference. While there have been thousands of SNe Ia studied to date (e.g., Jones et al. 2017), more examples are indeed still needed: there are only four normal, $z < 0.03$ SNe Ia in our sample, and these four are nearly as valuable as the entire remainder of the sample for establishing the diversity of SNe Ia. As low-z, high-cadence surveys improve our understanding of these priors, we can combine that knowledge with the hitherto unimaginable statistical samples from LSST (∼millions of SNe), to better understand the early evolution and rise time distribution of Type Ia SNe.

The authors would like to thank the anonymous referee for helpful comments that have improved this paper. We thank M. Magee for sharing details about the rise times of SNe Ia models. A. A. M. would like to thank E. A. Chase, M. Zevin, and C. P. L. Berry for useful discussions on KDEs and PDFs. We also appreciate D. Goldstein's suggestions regarding `SALT2` as a proxy for rise time. Y. Yang, J. Nordin, R. Biswas, and J. Sollerman provided detailed comments on an early draft that improved this manuscript.

A. A. M. is funded by the Large Synoptic Survey Telescope Corporation, the Brinson Foundation, and the Moore Foundation in support of the LSSTC Data Science Fellowship Program; he also receives support as a CIERA Fellow by the CIERA Postdoctoral Fellowship Program (Center for Interdisciplinary Exploration and Research in Astrophysics, Northwestern University). Y. Y., U. C. F., and S. R. K. thank the Heising-Simons Foundation for supporting ZTF research (#2018-0907). This research was supported in part through the computational resources and staff contributions provided for the Quest high-performance computing facility at Northwestern University, which is jointly supported by the Office of the Provost, the Office for Research, and Northwestern University Information Technology. This work was supported in part by the GROWTH project funded by the National Science Foundation under grant No. 1545949.

This work is based on observations obtained with the Samuel Oschin Telescope 48 inch and the 60 inch Telescope at the Palomar Observatory as part of the Zwicky Transient Facility project. ZTF is supported by the National Science Foundation under grant No. AST-1440341 and a collaboration including Caltech, IPAC, the Weizmann Institute for Science, the Oskar Klein Center at Stockholm University, the University of Maryland, the University of Washington, Deutsches Elektronen-Synchrotron and Humboldt University, Los Alamos National Laboratories, the TANGO Consortium of Taiwan, the University of Wisconsin at Milwaukee, and Lawrence Berkeley National Laboratories. Operations are conducted by COO, IPAC, and UW.

Software: `astropy` (Astropy Collaboration et al. 2013), `scipy` (Virtanen et al. 2020), `matplotlib` (Hunter 2007), `pandas` (McKinney 2010), `emcee` (Foreman-Mackey et al. 2013), `corner` (Foreman-Mackey 2016), `SALT2` (Guy et al. 2007), `sncosmo` (Barbary et al. 2016), `statsmodels` (Seabold & Perktold 2010).

Appendix A
Updated Priors Following the Change of Variables

As mentioned in Section 4, there is a strong degeneracy in the posterior estimates of A and α. This degeneracy can be removed under the change of variables from (A, α) to (A', α'), where $A' = A10^{\alpha}$ and $\alpha' = \alpha$. From the Jacobian of this transformation, we find

$$P(A', \alpha') = 10^{-\alpha'} P(A, \alpha).$$

The change in variables should not affect the prior probability, therefore

$$P(A', \alpha') = 10^{-\alpha'} P(A' 10^{-\alpha'}, \alpha'), \tag{A1}$$

which can be satisfied by:

$$P(A', \alpha') \propto A'^{-1} 10^{-\alpha'}. \tag{A2}$$

While Equation (A1) is also satisfied by $P(A', \alpha') \propto A'^{-1}$, adopting this as the joint prior on (A', α') does not remove the degeneracy between the parameters as A' absorbs the multiplicative factor of 10^{α}, effectively reducing the problem to be the same as it was before the change of variables. Thus, as listed in Table 2, we adopt Equation (A2) as the prior on the transformed variables, which we find breaks the degeneracy (see Figures 1–3).

Appendix B
Quality Assurance

As noted in Section 4, the MCMC model converges for all but one ZTF SNe within the sample. However, visual inspection of both the corner plots and individual draws from the posterior quickly reveals that, for some SNe, the data do not provide strong constraints on the model parameters (see Figure 3). In the most extreme cases, as shown in Figure B1, large gaps in the observations make it nearly impossible to

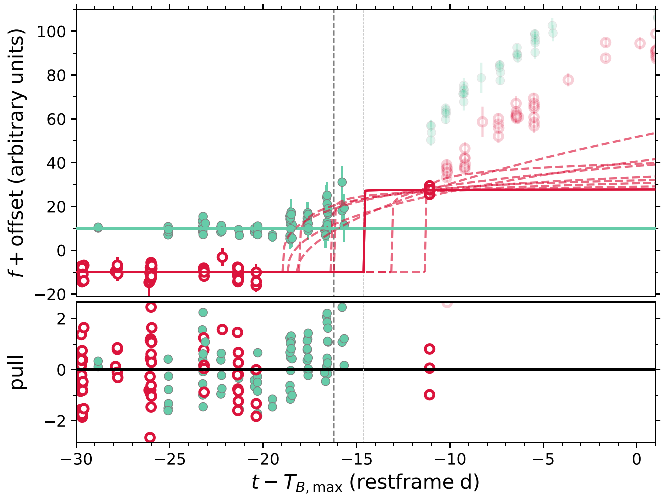

Figure B1. Same as the bottom panel of Figure 1 for ZTF18aaqffyp (SN 2018bhr), an SN with observations that place very weak constraints on t_{fl}. Marginalized posteriors for A' and α are essentially identical to the priors. Posteriors with little information beyond the prior are typical of SNe with significant observational gaps.

constrain the model parameters. For these cases, the model posteriors are essentially identical to the priors (there is always a weak constraint on t_{fl} from epochs where the SN is not detected).

To identify SNe with poor observational coverage, or unusual structure in the posterior, we visually examine the light curves and corner plots for each of the 127 SNe in our sample. We flag SNe where the model significantly underestimates the flux near $T_{B,\max}$ (similar to what is shown in Figure B1), as this is a good indicator that the model has poor predictive value. By definition, the light curve derivative is zero at maximum light, and the relative change in brightness constantly slows down in the week leading up to maximum light. Therefore, models of the early emission should greatly overpredict the flux at maximum, which is why we adopt this criterion for flagging SNe with poorly constrained model parameters.

Numerically, the visually flagged SNe can, for the most part, be identified by a combination of two criteria: the 90% credible region on t_{fl}, CR$_{90}$, and the number of nights on which the SN was detected. Rather than providing a threshold for detection (e.g., 3σ, 5σ, etc.), we count all nights with $f_{\rm mean} \leqslant 0.4 f_{\max}$ after the median marginalized posterior value of t_{fl} with observations in either the $g_{\rm ZTF}$, $r_{\rm ZTF}$, or both filters, $N_{g,\rm det}$, $N_{r,\rm det}$, and $N_{gr,\rm det}$, respectively. We take the geometric mean of these three numbers to derive the "average" number of nights on which the SN was detected, GM($N_{\rm det}$). A scatter plot showing GM($N_{\rm det}$) versus CR$_{90}$ is shown in Figure B2. Visually flagged SNe are shown as orange circles, while + symbols show those that were not flagged.

The visual inspection procedure described above is not fully reproducible (visual inspection is, by its very nature, subjective). Therefore, we aim to separate the SNe into two classes (reliable and unreliable) via an automated, systematic procedure. Treating the visually flagged sources as the negative class, we regard false positives (i.e., visually flagged SNe that are included in the final population analysis) to be particularly harmful. Therefore, we adopt

$$\mathrm{GM}(N_{\rm det}) \geqslant 1.9\, \mathrm{CR}_{90} + 1.65,$$

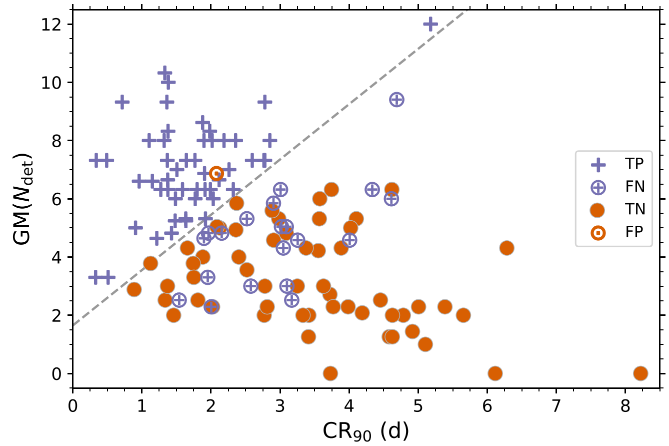

Figure B2. Scatter plot showing the distribution of the 127 ZTF SNe Ia in the GM($N_{\rm det}$)–CR$_{90}$ plane. Models with flagged posterior parameters are shown as orange circles, while those that are not flagged are shown via + symbols. The dashed line shows the adopted separation threshold for identifying reliable model fits (above the line), and unreliable model fits. FP and FN (see text) SNe are circled.

as the classification threshold for reliable model fits (as shown via the dashed line in Figure B2). This threshold retains 50 true positives (TP; visually good models included in the final sample) with only a single false positive (FP; visually flagged SNe in the final sample). This choice does result in 20 false negatives (FN; visually good models *excluded* from the final sample), while all remaining flagged SNe are true negatives (TN). Further scrutiny of the FN reveals several light curves with significant observational gaps—which, as discussed above, makes it difficult to place strong constraints on the model parameters. Ultimately, our two-step procedure identifies 51 SNe as reliable, while 76 are excluded from the final population analysis due to their unreliable constraints on the model parameters.

Appendix C
Rare and Unusual Thermonuclear SNe

In Yao et al. (2019), we identified six peculiar SNe Ia, which were classified as either SN 2002cx-like (hereafter 02cx-like or SN Iax), super-Chandrasekhar (SC) explosions, or SNe Ia interacting with their circumstellar medium (CSM), known as SN Ia-CSM. For this study, we have also excluded ZTF18abdmgab (SN 2018lph), a 1986G-like SN that would not typically be included in a sample used for cosmological studies. Here, we summarize the early evolution of these events.

For ZTF18abclfee (SN 2018cxk), an 02cx-like SN at $z = 0.029$, we obtained an exquisite sequence of observations in the time before explosion, as shown in Figure C1. According to the DIC, $\alpha \neq 2$ is decisively preferred for this SN. For ZTF18abclfee, we estimate[26] $t_{\rm rise}$=$10.01\pm^{0.40}_{0.33}$ days (the uncertainties represent the 90% credible region). This is the most precise measurement of the rise time of an 02cx-like SN to date. The only other 02cx-like event with good limits on the rise with deep upper limits is SN 2005hk (Phillips et al. 2007). SN 2005hk has a substantially longer rise time (∼15 days; see

[26] Rise times for the unusual SNe discussed in this appendix are measured relative to $T_{g,\max}$, as SALT2 does not provide reliable estimates of $T_{B,\max}$ for non-normal SNe Ia.

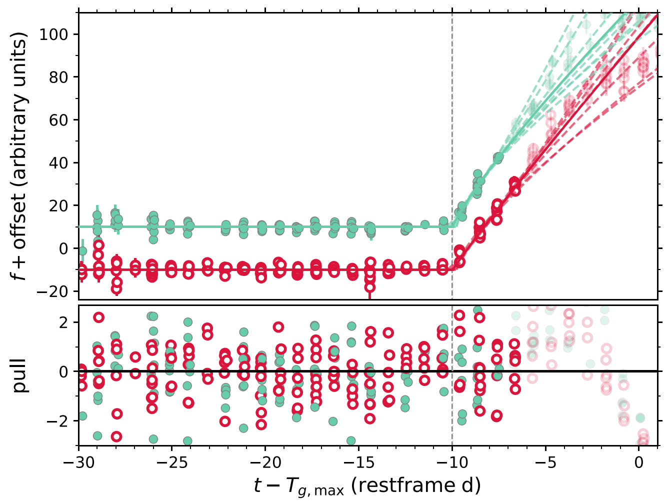

Figure C1. Same as the bottom panel of Figure 1 for ZTF18abclfee (SN 2018cxk), an 02cx-like SN with strong constraints on $t_{\rm fl}$, as well as a short rise time (∼10 days). ZTF18abclfee has the tightest constraints on $t_{\rm rise}$ of all 02cx-like SNe observed to date. The median 1D marginalized posterior value of $t_{\rm fl}$ and maximum *a posteriori* value of $t_{\rm fl}$ are nearly identical for ZTF18abclfee, so the thin gray line showing the latter is not visible.

Phillips et al. (2007)) than ZTF18abclfee, which is not surprising given that ZTF18abclfee is less luminous and declines more rapidly than SN 2005hk (Miller et al. 2017; Yao et al. 2019). ZTF18abclfee also exhibits a nearly linear early rise with $\alpha_g = 0.95^{0.32}_{0.19}$ and $\alpha_r = 0.98^{0.23}_{0.15}$.

ZTF18aaykjei (SN 2018crl), a Ia-CSM SN with $t_{\rm rise} = 22.8^{2.0}_{1.8}$ days and 26.3 ± 1 days for the uninformative and $\alpha = 2$ priors, respectively, has a significantly longer rise than the normal SNe in this study. Silverman et al. (2013) points out that Ia-CSM have exceptionally long rise times, and Firth et al. (2015) measure $t_{\rm rise} > 30$ days for two of the SNe in the Silverman et al. (2013) sample. We also note that the $r_{\rm ZTF}$ peak of ZTF18aaykjei occurs at least one week after the $g_{\rm ZTF}$ peak, as has been seen in other Ia-CSM SNe (Aldering et al. 2006; Prieto et al. 2007).

There are two SC SNe Ia (ZTF18abdpvnd/SN 2018dvf and ZTF18abhpgje/SN 2018eul) and two candidate SC SNe (ZTF18aawpcel/SN 2018cir and ZTF18abddmrf/SN 2018dsx) identified in Yao et al. (2019). Each of these events exhibits a long rise, ≳20 days and ≳25 days for the uninformative and $\alpha = 2$ priors, respectively, as previously seen in other SC events (e.g., Scalzo et al. 2010; Silverman et al. 2011). We note that, with the exception of ZTF18abdpvnd ($z = 0.05$), these events are detected at high redshift ($z \gtrsim 0.15$); as a result, the constraints on the individual rise time measurements are relatively weak.

Finally, for ZTF18abdmgab (SN 2018lph), the 86G-like SN identified in Yao et al. (2019), we cannot place strong constraints on the rise time, due to a significant gap in the observations around $t_{\rm fl}$.

Appendix D Systematics

D.1. Definition of "Early" for Model Fitting

In Section 4, we highlighted that there is no single agreed upon definition of which SN Ia observations are best for modeling the early evolution of SNe Ia. Throughout this study, we have adopted a threshold, $f_{\rm thresh}$, relative to the maximum observed flux, $f_{\rm max}$, whereby we define all observations less than $f_{\rm thresh} = 0.4$ the maximum in each filter ($f_{\rm obs} \leqslant 0.4 f_{\rm max}$) as the early portion of the light curve. As noted in Section 4, setting $f_{\rm thresh} = 0.4$, is arbitrary (although consistent with some previous studies). Here, we examine the effect of this particular choice if we had instead adopted $f_{\rm thresh} = 0.25$, 0.30, 0.35, 0.45, or 0.50 for the fitting procedure in Section 4.

There are 12 SNe for which the MCMC chains did not converge for one or more of the alternative flux thresholds. They are excluded from the analysis below. For the remaining 115 SNe in our sample, we consider the model parameters to be consistent if the marginalized, one-dimensional 90% credible regions for the three parameters that we care about, $t_{\rm fl}$, α_g, and α_r, overlap with the estimates when $f_{\rm thresh} = 0.40$.[27] This definition identifies substantial differences in the final model parameters while varying $f_{\rm thresh}$ over a reasonable range. Of the 115 SNe with converged chains, we find that 98 (>85% of the sample) have marginalized, 1D posterior credible regions consistent with the results for $f_{\rm thresh} = 0.40$, independent of the adopted value of $f_{\rm thresh}$. 15 of the 17 SNe that do not have consistent $t_{\rm fl}$, α_g, or α_r estimates feature gaps in observational coverage, which is the likely reason for the inconsistency. As $f_{\rm thresh}$ increases from 0.25 to 0.5, the information content dramatically changes before and after a gap leading to significantly different parameter estimates.

If we alternatively consider the results to be consistent only if the 68% credible regions agree with the $f_{\rm thresh} = 0.40$ results, then only 64 SNe have consistent parameters as $f_{\rm thresh}$ varies. This suggests that, while the results are largely consistent, the central mass of the posterior density is affected by which data are included or excluded in the model fit. In Figure D1, we show how the estimates of $t_{\rm fl}$ and α_g change as a function of $f_{\rm thresh}$ for SNe with consistent model parameters. Note that, by construction, the 90% credible regions for each SN overlap at every value of $f_{\rm thresh}$, and thus, for clarity, we omit error bars.

To identify trends with $f_{\rm thresh}$, we define SNe with both $\alpha_g(f_{\rm thresh} = 0.5)$ and $\alpha_g(f_{\rm thresh} = 0.45)$ greater than both $\alpha_g(f_{\rm thresh} = 0.25)$ and $\alpha_g(f_{\rm thresh} = 0.3)$ to show evidence for α_g increasing with $f_{\rm thresh}$. We define α_g as decreasing in cases where the opposite is true. Of the 98 SNe with consistent model parameters, 75 show evidence for α_g increasing with $f_{\rm thresh}$, while only seven show evidence for a decline. Using a similar definition for $t_{\rm rise}$ (note that decreasing $t_{\rm fl}$ corresponds to increasing $t_{\rm rise}$), we find that in 68 SNe $t_{\rm rise}$ increases with $f_{\rm thresh}$, while in 16 SNe $t_{\rm rise}$ decreases as more observations are included in the fit. Thus, the vast majority of SNe exhibit an increase in α_g and $t_{\rm fl}$ as $f_{\rm thresh}$ is increased. Figure D1 shows that the magnitude of this trend is much larger for α_g than $t_{\rm rise}$, which makes sense. When there are few SN detections, which is more likely when $f_{\rm thresh}$ is low, small values of α fit the data well, as in Figure B1. Including more information about the rise, by increasing $f_{\rm thresh}$, results in very low values of α no longer being consistent with the data. On the other hand, $t_{\rm fl}$ is strongly constrained by the first epoch of detection (see Section 6.2). In this case, the addition of more observations will not lead to as dramatic an effect.

[27] Given the strong correlation between α_g and α_r (see Section 6.1), we discuss only α_g below.

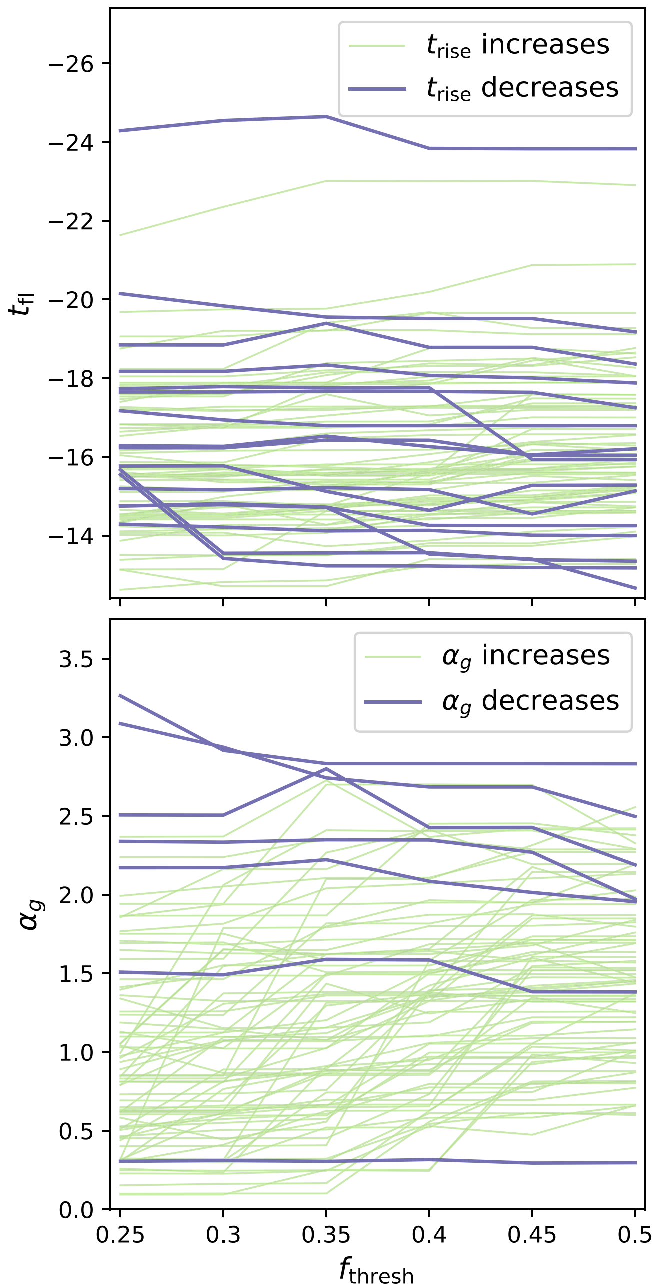

Figure D1. Evolution of the inferred values of $t_{\rm fl}$ and α_g as $f_{\rm thresh}$ is increased from 0.25 to 0.5. Only SNe with consistent model parameters, that nevertheless show evidence for increasing or decreasing with $f_{\rm thresh}$, are shown (see text for a definition of consistent, increasing, and decreasing). Thin green lines show SNe where $t_{\rm rise}$ or α_g increases as more observations are included in the model, while thick purple lines show SNe for which these values decline. We find that, for the vast majority of SNe, as additional observations are included in the model fit, both $t_{\rm rise}$ and α_g increase.

D.2. The Importance of Pre-explosion Observations

A unique and important component of our ZTF data set is the nightly collection of multiple observations. Yao et al. (2019) demonstrated that such an observational sequence enables low-S/N detections of the SN prior to the traditional 5σ discovery epoch (see Masci et al. 2019), which can provide critical constraints on $t_{\rm fl}$. Many previous studies have utilized filtered observations that were obtained ∼1 day or more after the epoch of discovery (e.g., Riess et al. 1999; Aldering et al. 2000; Ganeshalingam et al. 2011; Zheng et al. 2017). To demonstrate the importance of the ZTF subthreshold detections, we refit the model from Section 4 to each of our ZTF light curves after removing all observations before and on the night of the SN's first detection (i.e., S/N ⩾ 5, as defined in Yao et al. (2019)).

Following the removal of these observations, the MCMC chains converge (see Section 4) for only 10 SNe. This is understandable as the removal of the "baseline" observations makes it very difficult to constrain C_d and β_d. The removal of these observations leads to dramatically different estimates of the model parameters for these 10 SNe. Thus, we report the results given the strong trends, though we caution that these results are somewhat preliminary and should be confirmed with more detailed simulations.

With the baseline observations removed, the inferred value of $t_{\rm fl}$ increases (i.e., $t_{\rm rise}$ decreases) for all 10 SNe relative to the results from Section 4. The median difference of this shift is ∼3.5 days. Using the definition of agreement from Appendix D.1, i.e., overlap in the 90% credible regions, only three of the ten SNe have estimates of $t_{\rm fl}$ that agree after removing the nondetections. Removing the baseline observations also decreases estimates of α (which agrees with the trend seen in Figure 7), with only five of the ten SNe having estimates of α_g and α_r that agree. These trends suggest that pre-explosion observations are critically needed to produce accurate estimates of $t_{\rm rise}$ (see also González-Gaitán et al. 2012).

ORCID iDs

A. A. Miller https://orcid.org/0000-0001-9515-478X
Y. Yao https://orcid.org/0000-0001-6747-8509
M. Bulla https://orcid.org/0000-0002-8255-5127
C. Pankow https://orcid.org/0000-0002-1128-3662
E. C. Bellm https://orcid.org/0000-0001-8018-5348
S. B. Cenko https://orcid.org/0000-0003-1673-970X
R. Dekany https://orcid.org/0000-0002-5884-7867
C. Fremling https://orcid.org/0000-0002-4223-103X
M. J. Graham https://orcid.org/0000-0002-3168-0139
T. Kupfer https://orcid.org/0000-0002-6540-1484
R. R. Laher https://orcid.org/0000-0003-2451-5482
A. A. Mahabal https://orcid.org/0000-0003-2242-0244
F. J. Masci https://orcid.org/0000-0002-8532-9395
P. E. Nugent https://orcid.org/0000-0002-3389-0586
R. Riddle https://orcid.org/0000-0002-0387-370X
B. Rusholme https://orcid.org/0000-0001-7648-4142
R. M. Smith https://orcid.org/0000-0001-7062-9726
D. L. Shupe https://orcid.org/0000-0003-4401-0430
J. van Roestel https://orcid.org/0000-0002-2626-2872
S. R. Kulkarni https://orcid.org/0000-0001-5390-8563

References

Akaike, H. 1974, IEEE Trans., 19, 6
Aldering, G., Antilogus, P., Bailey, S., et al. 2006, ApJ, 650, 510
Aldering, G., Knop, R., & Nugent, P. 2000, AJ, 119, 2110
Amanullah, R., Lidman, C., Rubin, D., et al. 2010, ApJ, 716, 712
Arnett, W. D. 1982, ApJ, 253, 785
Astropy Collaboration, Robitaille, T. P., Tollerud, E. J., Greenfield, P., et al. 2013, A&A, 558, A33
Barbary, K., Barclay, T., Biswas, R., et al. 2016, SNCosmo: Python Library for Supernova Cosmology, Astrophysics Source Code Library, ascl:1611.017
Bellm, E. C., Kulkarni, S. R., Barlow, T., et al. 2019a, PASP, 131, 068003
Bellm, E. C., Kulkarni, S. R., Graham, M. J., et al. 2019b, PASP, 131, 018002
Bianco, F. B., Howell, D. A., Sullivan, M., et al. 2011, ApJ, 741, 20

Blondin, S., Dessart, L., Hillier, D. J., & Khokhlov, A. M. 2013, MNRAS, 429, 2127
Bloom, J. S., Kasen, D., Shen, K. J., et al. 2012, ApJL, 744, L17
Bulla, M., Miller, A. A., Yao, Y., et al. 2020, ApJ,
Cai, T. T. 2005, J. Stat. Plan. Inf., 131, 63
Cao, Y., Kulkarni, S. R., Howell, D. A., et al. 2015, Natur, 521, 328
Clopper, C. J., & Pearson, E. S. 1934, Biometrika, 26, 404
Conley, A., Howell, D. A., Howes, A., et al. 2006, AJ, 132, 1707
De, K., Kasliwal, M. M., Polin, A., et al. 2019, ApJL, 873, L18
Dekany, R., Smith, R. M., Riddle, R., et al. 2020, PASP, 132, 038001
Dessart, L., Blondin, S., Hillier, D. J., & Khokhlov, A. 2014, MNRAS, 441, 532
Dilday, B., Howell, D. A., Cenko, S. B., et al. 2012, Sci, 337, 942
Dimitriadis, G., Foley, R. J., Rest, A., et al. 2019, ApJL, 870, L1
Fausnaugh, M. M., Vallely, P. J., Kochanek, C. S., et al. 2019, arXiv:1904.02171
Firth, R. E., Sullivan, M., Gal-Yam, A., et al. 2015, MNRAS, 446, 3895
Foreman-Mackey, D. 2016, JOSS, 1, 24
Foreman-Mackey, D., Hogg, D. W., Lang, D., & Goodman, J. 2013, PASP, 125, 306
Ganeshalingam, M., Li, W., & Filippenko, A. V. 2011, MNRAS, 416, 2607
Gelman, A., Hwang, J., & Vehtari, A. 2014, Stat. Comput., 24, 997
González-Gaitán, S., Conley, A., Bianco, F. B., et al. 2012, ApJ, 745, 44
Goobar, A., Kromer, M., Siverd, R., et al. 2015, ApJ, 799, 106
Goodman, J., & Weare, J. 2010, CAMCS, 5, 65
Graham, M. J., Kulkarni, S. R., Bellm, E. C., et al. 2019, PASP, 131, 078001
Gronow, S., Collins, C., Ohlmann, S. T., et al. 2020, A&A, 635, A169
Guy, J., Astier, P., Baumont, S., et al. 2007, A&A, 466, 11
Hayden, B., Rubin, D., & Strovink, M. 2019, ApJ, 871, 219
Hayden, B. T., Garnavich, P. M., Kessler, R., et al. 2010, ApJ, 712, 350
Hogg, D. W., Bovy, J., & Lang, D. 2010, arXiv:1008.4686H
Hosseinzadeh, G., Sand, D. J., Valenti, S., et al. 2017, ApJL, 845, L11
Howell, S. B., Sobeck, C., Haas, M., et al. 2014, PASP, 126, 398
Hunter, J. D. 2007, CSE, 9, 90
Ivezić, Ž., Kahn, S. M., Tyson, J. A., et al. 2019, ApJ, 873, 111
Jeffery, D. J. 1999, arXiv:9907015
Jeffreys, H. 1946, RSPSA, 186, 453
Jeffreys, H. 1961, Theory of Probability (3rd ed.; Oxford: Clarendon)
Jiang, J.-A., Doi, M., Maeda, K., et al. 2017, Natur, 550, 80
Jones, D. O., Scolnic, D. M., Foley, R. J., et al. 2019, ApJ, 881, 19
Jones, D. O., Scolnic, D. M., Riess, A. G., et al. 2017, ApJ, 843, 6
Kasen, D. 2010, ApJ, 708, 1025
Kasliwal, M. M., Cannella, C., Bagdasaryan, A., et al. 2019, PASP, 131, 038003
Kromer, M., Fremling, C., Pakmor, R., et al. 2016, MNRAS, 459, 4428
Levanon, N., & Soker, N. 2017, MNRAS, 470, 2510
Livio, M., & Mazzali, P. 2018, PhR, 736, 1
Magee, M. R., & Maguire, K. 2020, arXiv:2007.02101
Magee, M. R., Maguire, K., Kotak, R., et al. 2020, A&A, 634, A37
Magee, M. R., Sim, S. A., Kotak, R., & Kerzendorf, W. E. 2018, A&A, 614, A115
Maoz, D., Mannucci, F., & Nelemans, G. 2014, ARA&A, 52, 107
Marion, G. H., Brown, P. J., Vinkó, J., et al. 2016, ApJ, 820, 92
Masci, F. J., Laher, R. R., Rusholme, B., et al. 2019, PASP, 131, 018003
McKinney, W. 2010, in Proc. 9th Python in Science Conf., 51
Miller, A. A., Cao, Y., Piro, A. L., et al. 2018, ApJ, 852, 100
Miller, A. A., Kasliwal, M. M., Cao, Y., et al. 2017, ApJ, 848, 59
Miller, A. A., Magee, M. R., Polin, A., et al. 2020, ApJ, 898, 56
Noebauer, U. M., Kromer, M., Taubenberger, S., et al. 2017, MNRAS, 472, 2787
Nomoto, K. 1982a, ApJ, 253, 798
Nomoto, K. 1982b, ApJ, 257, 780
Nugent, P. E., Sullivan, M., Cenko, S. B., et al. 2011, Natur, 480, 344
Olling, R. P., Mushotzky, R., Shaya, E. J., et al. 2015, Natur, 521, 332
Papadogiannakis, S., Goobar, A., Amanullah, R., et al. 2019, MNRAS, 483, 5045
Parrent, J. T., Howell, D. A., Friesen, B., et al. 2012, ApJL, 752, L26
Pedregosa, F., Varoquaux, G., Gramfort, A., et al. 2011, JMLR, 12, 2825
Perlmutter, S., Aldering, G., Goldhaber, G., et al. 1999, ApJ, 517, 565
Phillips, M. M. 1993, ApJL, 413, L105
Phillips, M. M., Li, W., Frieman, J. A., et al. 2007, PASP, 119, 360
Piro, A. L., & Morozova, V. S. 2016, ApJ, 826, 96
Piro, A. L., & Nakar, E. 2013, ApJ, 769, 67
Piro, A. L., & Nakar, E. 2014, ApJ, 784, 85
Polin, A., Nugent, P., & Kasen, D. 2019, ApJ, 873, 84
Prieto, J. L., Garnavich, P. M., Phillips, M. M., et al. 2007, arXiv:0706.4088
Ricker, G. R., Winn, J. N., Vanderspek, R., et al. 2015, JATIS, 1, 014003
Riess, A. G., Filippenko, A. V., Challis, P., et al. 1998, AJ, 116, 1009
Riess, A. G., Filippenko, A. V., Li, W., et al. 1999, AJ, 118, 2675
Riess, A. G., Macri, L. M., Hoffmann, S. L., et al. 2016, ApJ, 826, 56
Scalzo, R. A., Aldering, G., Antilogus, P., et al. 2010, ApJ, 713, 1073
Scalzo, R. A., Ruiter, A. J., & Sim, S. A. 2014, MNRAS, 445, 2535
Schwarz, G. 1978, AnSta, 6, 461
Scolnic, D. M., Jones, D. O., Rest, A., et al. 2018, ApJ, 859, 101
Seabold, S., & Perktold, J. 2010, in Proc. 9th Python in Science Conf., 92
Shappee, B. J., Holoien, T. W. S., Drout, M. R., et al. 2019, ApJ, 870, 13
Shappee, B. J., Piro, A. L., Holoien, T. W.-S., et al. 2016, ApJ, 826, 144
Shappee, B. J., Piro, A. L., Stanek, K. Z., et al. 2018, ApJ, 855, 6
Shen, K. J., Boubert, D., Gänsicke, B. T., et al. 2018, ApJ, 865, 15
Silverman, J. M., Ganeshalingam, M., Li, W., et al. 2011, MNRAS, 410, 585
Silverman, J. M., Nugent, P. E., Gal-Yam, A., et al. 2013, ApJS, 207, 3
Sim, S. A., Seitenzahl, I. R., Kromer, M., et al. 2013, MNRAS, 436, 333
Soker, N., Kashi, A., García-Berro, E., et al. 2013, MNRAS, 431, 1541
Spiegelhalter, D. J., Best, N. G., Carlin, B. P., & van der Linde, A. 2002, J. R. Stat. Soc. Ser. B., 64, 583
Townsley, D. M., Miles, B. J., Shen, K. J., & Kasen, D. 2019, ApJL, 878, L38
Virtanen, P., Gommers, R., Oliphant, T. E., et al. 2020, NatMethod., 17, 261
Webbink, R. F. 1984, ApJ, 277, 355
Whelan, J., & Iben, I. J. 1973, ApJ, 186, 1007
Yao, Y., Miller, A. A., Kulkarni, S. R., et al. 2019, ApJ, 886, 152
Zackay, B., Ofek, E. O., & Gal-Yam, A. 2016, ApJ, 830, 27
Zheng, W., & Filippenko, A. V. 2017, ApJL, 838, L4
Zheng, W., Kelly, P. L., & Filippenko, A. V. 2017, ApJ, 848, 66
Zheng, W., Shivvers, I., Filippenko, A. V., et al. 2014, ApJL, 783, L24
Zheng, W., Silverman, J. M., Filippenko, A. V., et al. 2013, ApJL, 778, L15